Turbulence measurements by wind lidars

Ameya Sathe and Jakob Mann
DTU Wind Energy, Risø Campus, Roskilde, Denmark

1 Introduction

Turbulence is the chaotic, ever-changing, three-dimensional nature of a fluid flow. If say we are in a dream world, where we had infinite computing power, and the initial and boundary flow conditions were perfectly known then the fluid flow can be mathematically solved using the time domain Navier-Stokes (NS) equations, and hence we could mathematically capture turbulence perfectly. Life would be much simpler and we would never need to measure any flow using any instrument, leave aside using complicated instruments such as lidars. In this dream world when we would for example design wind turbines then we can perfectly determine the loads, and the safety factors that influence how much extra material should be used for manufacturing different wind turbine components will be drastically reduced, resulting in the cheapest wind turbine that can ever be produced.

Unfortunately, we live in a real world, where none of the above requirements are fulfilled, and we are forced to understand turbulence using different techniques. In our imperfect world then the need for measurements is inevitable. A practical way to measure turbulence is to have an instrument like sonic anemometer installed on a meteorological mast at different points in space (usually in the vertical direction). They are currently the best available instruments to measure turbulence with some caveats attached. Tall meteorological masts are required in order to measure high up in the atmosphere, which increase the cost of measurement, particularly under offshore conditions. Flow distortions from the mast and the sonics have also to be taken into account rendering them unusable under certain wind directions. As an alternative, wind lidars offer a tremendous opportunity for measuring wind remotely. These lidars do not need a mast and we do not have to worry about flow distortions.

However, there are other problems that arise by the use of lidars to measure turbulence, particularly using the velocity azimuth display (VAD) technique. These problems are discussed in the following sections for the continuous-wave (CW) and pulsed lidars.

2 Measurement of turbulence using VAD technique

Fig. 1 shows the lidar emitting the laser beam at different azimuth angles θ. The azimuth angles increase from 0°–360° in the clockwise direction as for the geographical convention. The line-of-sight velocity (also called radial velocity v_r) is measured by the lidar at each azimuth angle. The half-opening angle ϕ (= 90° − elevation angle) is kept constant throughout the scan. The CW and pulsed lidars work on the principle of backscattering of the emitted radiation, and subsequent detection of the Doppler shift in the frequency of the received radiation. The Doppler shift in the frequency is related to v_r by,

$$\delta f = 2\frac{v_r}{\lambda}, \tag{1}$$

where f and λ are the frequency and wavelength of the emitted radiation. Mathematically, v_r is given as the dot product of the unit directional vector and the velocity field at the point of focus

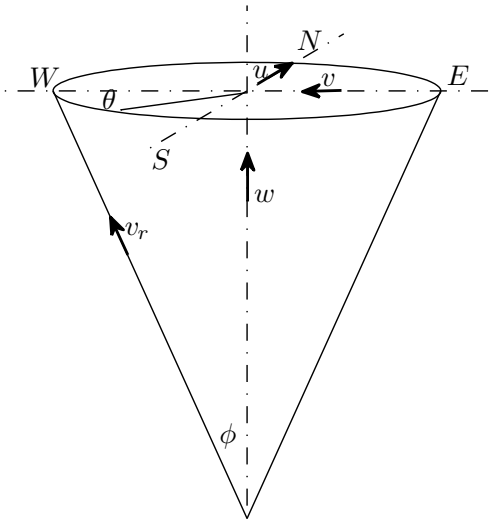

Figure 1: Schematic of the velocity azimuth display scanning

for a CW lidar, and the center of the range gate (Lindelöw, 2007) for the pulsed lidar,

$$v_r(\theta) = \boldsymbol{n}(\theta) \cdot \mathbf{v}(d_f \boldsymbol{n}(\theta)), \tag{2}$$

where d_f is the focus distance for the CW lidar or the distance to the center of the range gate for the pulsed lidar at which the wind speeds are measured, $\mathbf{v} = (u, v, w)$ is the instantaneous velocity field evaluated at the focus point or the center of the range gate $d_f \boldsymbol{n}(\theta)$, and $\boldsymbol{n}(\theta)$ is the unit directional vector given as,

$$\boldsymbol{n}(\theta) = (\cos\theta \sin\phi, \sin\theta \sin\phi, \cos\phi). \tag{3}$$

In practice it is impossible to obtain the backscattered radiation precisely from only the focus point, and there is always backscattered radiation of different intensities from different regions in space along the line-of-sight. Hence, it is necessary to assign appropriate weights to the backscattered intensity such that the weight corresponding to the focus point or the center of the range gate is the highest. Mathematically, the weighted average radial velocity can be written as,

$$\tilde{v}_r(\theta) = \int_{-\infty}^{\infty} \varphi(s) \boldsymbol{n}(\theta) \cdot \mathbf{v}(s\boldsymbol{n}(\theta) + d_f \boldsymbol{n}(\theta))\, ds, \tag{4}$$

where $\varphi(s)$ is any weighting function, integrating to one, and s is the distance along the beam from the focus or the center of the range gate. For simplicity we assume that $s = 0$ corresponds to the focus distance or center of the range gate.

2.1 Reynolds stress tensor measurements

Mathematically, the Reynolds stress tensor R_{ij} can be represented as a 3×3 matrix of second-order statistics of wind field components,

$$R_{ij} = \begin{bmatrix} \langle u'^2 \rangle & \langle u'v' \rangle & \langle u'w' \rangle \\ \langle v'u' \rangle & \langle v'^2 \rangle & \langle v'w' \rangle \\ \langle w'u' \rangle & \langle w'v' \rangle & \langle w'^2 \rangle \end{bmatrix} \tag{5}$$

In this section, we first present modelling of the components of R_{ij} as measured by a scanning lidar, and then we compare our model with the measurements. Modelling will help us in understanding roughly the mechanism of measurement of R_{ij} using lidars under VAD technique. Any model is normally build on a certain set of assumptions. This is not a strict requirement but rather our inability to construct an exact model without making use of any assumptions. Thus, the assumptions then become quite central in developing a model. Following are the main assumptions of our model:

1. Turbulence is horizontally homogeneous within the scanning area – This means that R_{ij} remains constant on any point on a scanning circle. Without this assumption the mathematics becomes quite complex, and we currently do have tools to tackle such a problem.

2. The flow field is frozen during the scan – This means that turbulence is advected only by the mean flow. This gives a direct connection between the spatial and temporal scales of turbulence. Without this assumption, we will have to take care of space-time correlations, and again the mathematics become quite complex, which we are not able to handle it currently.

3. Eq. (4) with an appropriately chosen $\varphi(s)$ models the averaging well – This assumption directly influences the amount of averaging of turbulence scales that occurs within the sample volume of a lidar measurement. The choice of $\varphi(s)$ then becomes very important. Fortunately, studies have been carried out previously to model $\varphi(s)$ for CW and pulsed lidars, and in our model we simply use the results from such studies.

4. The spatial structure of the turbulent flow is described well by the spectral tensor model of Mann (1994) – At this stage it is quite difficult to explain the significance of this assumption but its importance will become more prominent as we develop our model and make comparisons with the measurements. For now, it is just important to know that this assumption is quite central while making comparisons of the theoretical calculations with the measurements.

At this point we would like to reiterate that the modelling carried out in this section only helps to understand the measurement of R_{ij} by lidars using the VAD technique.

2.1.1 Modelling of R_{ij} for the CW lidar

In our study we have used the ZephIR (manufactured by Natural Power) as a CW lidar. Thus to construct a model it is necessary to know the exact measurement technique used by the ZephIR. The ZephIR transmits the laser beam through a constantly rotating prism, giving the required half-opening angle of nominally 30°. Each of up to five heights are scanned for one or three seconds, corresponding to one or three complete rotations of the prism. The beam is then re-focused to the next height in the sequence and the scanning procedure is repeated. Up to five different heights can be selected, the sequence (with five heights and three second scans) taking up to 18 seconds to complete. Thus the lidar spends less than 20% of the time required to make a wind profile on any one of the five heights. A typical scan at each height consists of 50 measurements of v_r on the azimuth circle. If we assume the coordinate system such that u is aligned to the mean wind direction, v is perpendicular to the mean wind direction, w is the vertical component, and the mean wind comes from the North then $\tilde{v}_r(\theta)$ can be expressed as,

$$\tilde{v}_r(\theta) = A + B\cos\theta + C\sin\theta, \tag{6}$$

where the coefficients $A = w_{qq}\ \cos\phi$, $B = u_{qq}\ \sin\phi$ and $C = v_{qq}\ \sin\phi$ and the sign ambiguity in $\tilde{v}_r(\theta)$ is neglected (see Mann et al. (2010)). We use the subscript qq to denote the velocity components measured by ZephIR, since they are not the true velocity components u, v and w. The assumption that the mean wind comes from the North is only made for simplicity. For a lidar

measuring at many points on the azimuth circle the choice of the mean wind direction does not matter since averaging over the entire circle is carried out. The values of the coefficients A, B and C are found using least squares method by fitting Eq. (6) to the measured values of $\tilde{v}_r(\theta)$ at all scanned azimuth angles. The coefficients can be written as Fourier integrals,

$$A = \frac{1}{2\pi}\int_0^{2\pi} \tilde{v}_r(\theta)\ d\theta, \tag{7}$$

$$B = \frac{1}{\pi}\int_0^{2\pi} \tilde{v}_r(\theta)\ \cos\theta\ d\theta, \tag{8}$$

$$C = \frac{1}{\pi}\int_0^{2\pi} \tilde{v}_r(\theta)\ \sin\theta\ d\theta. \tag{9}$$

We proceed by deriving expressions for the w_{qq} variance. The expressions for the (co-) variances of the remaining components of wind velocity can be derived in a similar manner.

The variance of A is defined as $\sigma_A^2 = \langle A'^2 \rangle$, where $\langle\rangle$ denotes ensemble averaging of a variable. From the above definition of A we can write,

$$\sigma_A^2 = \langle w_{qq}'^2 \rangle \cos^2\phi. \tag{10}$$

Using Eq. (7) we can also write,

$$\sigma_A^2 = \left\langle \left(\frac{1}{2\pi}\int_0^{2\pi} \tilde{v}_r'(\theta)\ d\theta \right)^2 \right\rangle. \tag{11}$$

Substituting $\tilde{v}_r(\theta)$ from Eq. (4) into Eq. (11), converting the square of the integral into a double integral, interchanging the order of integration and averaging we get,

$$\begin{aligned}\sigma_A^2 =& \frac{1}{4\pi^2}\int_0^{2\pi}\int_0^{2\pi}\int_{-\infty}^{\infty}\int_{-\infty}^{\infty} \langle \mathrm{v}_i'(s_1\boldsymbol{n}(\theta_1) + d_f\boldsymbol{n}(\theta_1))\mathrm{v}_j'(s_2\boldsymbol{n}(\theta_2) + d_f\boldsymbol{n}(\theta_2))\rangle \\ & \varphi(s_1)\varphi(s_2)n_i(\theta_1)n_j(\theta_2)\ ds_1 ds_2 d\theta_1 d\theta_2, \\ =& \frac{1}{4\pi^2}\int_0^{2\pi}\int_0^{2\pi}\int_{-\infty}^{\infty}\int_{-\infty}^{\infty} R_{ij}(\boldsymbol{r})\varphi(s_1)\varphi(s_2)n_i(\theta_1)n_j(\theta_2)\ ds_1 ds_2 d\theta_1 d\theta_2,\end{aligned} \tag{12}$$

where $\langle \mathrm{v}_i'(s_1\boldsymbol{n}(\theta_1) + d_f\boldsymbol{n}(\theta_1))\mathrm{v}_j'(s_2\boldsymbol{n}(\theta_2) + d_f\boldsymbol{n}(\theta_2))\rangle = R_{ij}(\boldsymbol{r})$ is the covariance tensor separated by a distance $\boldsymbol{r} = (s_1\boldsymbol{n}(\theta_1) + d_f\boldsymbol{n}(\theta_1)) - (s_2\boldsymbol{n}(\theta_2) + d_f\boldsymbol{n}(\theta_2))$ and is related to the three dimensional spectral velocity tensor $\Phi_{ij}(\boldsymbol{k})$ by the inverse Fourier transform,

$$R_{ij}(\boldsymbol{r}) = \int \Phi_{ij}(\boldsymbol{k}) e^{\mathrm{i}\boldsymbol{k}\cdot\boldsymbol{r}}\ d\boldsymbol{k}, \tag{13}$$

where $\int d\boldsymbol{k} \equiv \int_{-\infty}^{\infty}\int_{-\infty}^{\infty}\int_{-\infty}^{\infty} dk_1 dk_2 dk_3$, $\boldsymbol{k} = (k_1, k_2, k_3)$ denotes the wave vector and the subscripts i, j take the values from 1 to 3. Inserting Eq. (13) into Eq. (12) we get,

$$\begin{aligned}\sigma_A^2 = \int \Phi_{ij}(\boldsymbol{k}) & \left(\int_{-\infty}^{\infty} \varphi(s_1) \left[\frac{1}{2\pi}\int_0^{2\pi} n_i(\theta_1) e^{\mathrm{i}(s_1 + d_f)\boldsymbol{k}\cdot\boldsymbol{n}(\theta_1)}\ d\theta_1 \right] ds_1 \right) \\ & \left(\int_{-\infty}^{\infty} \varphi(s_2) \left[\frac{1}{2\pi}\int_0^{2\pi} n_j(\theta_2) e^{-\mathrm{i}(s_2 + d_f)\boldsymbol{k}\cdot\boldsymbol{n}(\theta_2)}\ d\theta_2 \right] ds_2 \right)\ d\boldsymbol{k}.\end{aligned} \tag{14}$$

Let $\alpha_i(\boldsymbol{k}) = \left(\int_{-\infty}^{\infty} \varphi(s) \left[\frac{1}{2\pi}\int_0^{2\pi} n_i(\theta) e^{\mathrm{i}(s + d_f)\boldsymbol{k}\cdot\boldsymbol{n}(\theta)}\ d\theta \right] ds \right)$, which physically represents the line-of-sight and conical averaging. Eq. (14) can then be written as (using Eq. 10),

$$\langle w_{qq}'^2 \rangle \cos^2\phi = \int \Phi_{ij}(\boldsymbol{k})\alpha_i(\boldsymbol{k})\alpha_j^*(\boldsymbol{k})\ d\boldsymbol{k}, \tag{15}$$

where $*$ denotes complex conjugation. Thus the integral reduces to evaluating $\alpha_i(\boldsymbol{k})$, since the analytical expressions for $\Phi_{ij}(\boldsymbol{k})$ are given in Mann (1994). Eq. (15) can then be estimated numerically. For a CW lidar, $\varphi(s)$ is well approximated by a Lorentzian function (Sonnenschein and Horrigan, 1971),

$$\varphi(s) = \frac{1}{\pi}\frac{l}{l^2+s^2}, \tag{16}$$

where l is the Rayleigh length ($= \lambda_b d_f^2/\pi r_b^2$, where $\lambda_b = 1.55$ μm is the wavelength of the emitted radiation, and $r_b = 19.5$ mm is the beam radius). An attempt has been made to obtain analytical expressions for $\alpha_i(\boldsymbol{k})$. However, no general analytical solution exists for $\alpha_i(\boldsymbol{k})$ and at most the integral can be reduced (by integrating over s) to

$$\alpha_i(\boldsymbol{k}) = \frac{1}{2\pi}\, e^{\mathrm{i}d_f k_3 \cos\phi} \int_0^{2\pi} n_i(\theta+\theta_0)\; e^{\mathrm{i}d_f k_h \sin\phi\cos\theta}\; e^{-l|k_h\cos\theta\sin\phi + k_3\cos\phi|}\; d\theta, \tag{17}$$

where $k_h = \sqrt{k_1^2+k_2^2}$ is the magnitude of the horizontal wave vector, $\cos\theta_0 = k_1/k_h$, $\sin\theta_0 = k_2/k_h$, and $n_i(\theta+\theta_0)$ is the component of the unit directional vector obtained from Eq. (3). Thus numerical integration has to be applied also for the evaluation of $\alpha_i(\boldsymbol{k})$.

A similar approach is taken for deriving u_{qq} and v_{qq} variances, where we obtain,

$$\langle u_{qq}'^2\rangle \sin^2\phi = \int \Phi_{ij}(\boldsymbol{k})\beta_i(\boldsymbol{k})\beta_j^*(\boldsymbol{k})\; d\boldsymbol{k}, \tag{18}$$

$$\langle v_{qq}'^2\rangle \sin^2\phi = \int \Phi_{ij}(\boldsymbol{k})\gamma_i(\boldsymbol{k})\gamma_j^*(\boldsymbol{k})\; d\boldsymbol{k}. \tag{19}$$

The corresponding β and γ functions are,

$$\beta_i(\boldsymbol{k}) = \frac{1}{\pi}\, e^{\mathrm{i}d_f k_3\cos\phi} \int_0^{2\pi} n_i(\theta+\theta_0)\cos(\theta+\theta_0)\; e^{\mathrm{i}d_f k_h\sin\phi\cos\theta}\; e^{-l|k_h\cos\theta\sin\phi+k_3\cos\phi|}\; d\theta, \tag{20}$$

$$\gamma_i(\boldsymbol{k}) = \frac{1}{\pi}\, e^{\mathrm{i}d_f k_3\cos\phi} \int_0^{2\pi} n_i(\theta+\theta_0)\sin(\theta+\theta_0)\; e^{\mathrm{i}d_f k_h\sin\phi\cos\theta}\; e^{-l|k_h\cos\theta\sin\phi+k_3\cos\phi|}\; d\theta. \tag{21}$$

The derivation of the co-variances is merely a combination of the weighting functions $\alpha_i(\boldsymbol{k})$, $\beta_i(\boldsymbol{k})$, $\gamma_i(\boldsymbol{k})$ and their complex conjugates used with $\Phi_{ij}(\boldsymbol{k})$. Since the ZephIR scans three circles in approximately three seconds, there will be a low-pass filter effect in turbulence measurements. We assume a length scale $L_f = \langle u\rangle \times 3$s such that it represents the three seconds averaging. We assume that the ZephIR scans a circle infinitely fast for three seconds. We model the corresponding filtering effect by a simple rectangular filter, such that,

$$f(x) = \begin{cases} \frac{1}{L_f} & \text{for } |x| < \frac{L_f}{2}; \\ 0 & \text{elsewhere,} \end{cases} \tag{22}$$

where x is the center of the scanning circle and $f(x)$ is any function of x. The corresponding spectral transfer function is given as,

$$\hat{T}_f(k_1) = \mathrm{sinc}^2\left(\frac{k_1 L_f}{2}\right), \tag{23}$$

where $\mathrm{sinc}(x) = \sin(x)/x$. The variances of u_{qq}, v_{qq} and w_{qq} are given as,

$$\langle u'^2_{qq} \rangle \sin^2\phi = \int \Phi_{ij}(\boldsymbol{k}) \beta_i(\boldsymbol{k}) \beta_j^*(\boldsymbol{k}) \hat{T}_f(k_1)\ d\boldsymbol{k}, \tag{24}$$

$$\langle v'^2_{qq} \rangle \sin^2\phi = \int \Phi_{ij}(\boldsymbol{k}) \gamma_i(\boldsymbol{k}) \gamma_j^*(\boldsymbol{k}) \hat{T}_f(k_1)\ d\boldsymbol{k}, \tag{25}$$

$$\langle w'^2_{qq} \rangle \cos^2\phi = \int \Phi_{ij}(\boldsymbol{k}) \alpha_i(\boldsymbol{k}) \alpha_j^*(\boldsymbol{k}) \hat{T}_f(k_1)\ d\boldsymbol{k}. \tag{26}$$

2.1.2 Modelling of R_{ij} for the pulsed lidar

The assumption made in section 2.1.1 that the mean wind direction comes from the North cannot be made for the WindCube, since it measures at four azimuth angles only (refer Fig. 1), e.g. North, East, South and West. In this case the coordinate system is such that u is aligned in the mean wind direction. Thus,

$$u_{wc} = u_{NS}\cos\Theta + u_{EW}\sin\Theta, \tag{27}$$

$$v_{wc} = u_{NS}\sin\Theta - u_{EW}\cos\Theta, \tag{28}$$

where u_{NS} and u_{EW} denote wind speeds in the North-South and East-West directions respectively, Θ denotes the wind direction, and the subscript wc denotes the velocity components measured by WindCube. From simple geometrical considerations (refer Fig. 1),

$$u_{NS} = \frac{\tilde{v}_{rN} - \tilde{v}_{rS}}{2\sin\phi}, \tag{29}$$

$$u_{EW} = \frac{\tilde{v}_{rE} - \tilde{v}_{rW}}{2\sin\phi}, \tag{30}$$

where $\tilde{v}_{rN}$, $\tilde{v}_{rS}$, $\tilde{v}_{rE}$, $\tilde{v}_{rW}$ are the weighted average radial velocities in the North, South, East and West directions respectively. For the w component,

$$w_{wc} = \frac{P(\tilde{v}_{rN} + \tilde{v}_{rS}) + Q(\tilde{v}_{rE} + \tilde{v}_{rW})}{2\cos\phi}, \tag{31}$$

where P and Q are the weights associated with the wind direction such that $P + Q = 1$. Leosphere uses $P = \cos^2\Theta$ and $Q = \sin^2\Theta$, and hence, we use the same in our calculations.

We proceed by deriving expressions for the u_{wc} variance. The expressions for the (co-) variances of the remaining components of wind velocity can be derived in a similar manner. Substituting Eqs. (29), (30) into Eq. (27) we get,

$$u_{wc} = \frac{1}{2\sin\phi}[(\tilde{v}_{rN} - \tilde{v}_{rS})\cos\Theta + (\tilde{v}_{rE} - \tilde{v}_{rW})\sin\Theta]. \tag{32}$$

We define unit vectors in the four directions as,

$$\begin{aligned} \boldsymbol{n}_N &= \boldsymbol{n}(-\Theta), \\ \boldsymbol{n}_S &= \boldsymbol{n}(\pi - \Theta), \\ \boldsymbol{n}_E &= \boldsymbol{n}(\frac{\pi}{2} - \Theta), \\ \boldsymbol{n}_W &= \boldsymbol{n}(\frac{3\pi}{2} - \Theta), \end{aligned} \tag{33}$$

where $\boldsymbol{n}_N$, $\boldsymbol{n}_S$, $\boldsymbol{n}_E$ and $\boldsymbol{n}_W$ are the unit directional vectors in the North, South, East and West directions respectively. From Eq. (4), for the North direction,

$$\tilde{v}_{rN} = \int_{-\infty}^{\infty} \varphi(s)\boldsymbol{n}_N \cdot \mathbf{v}(s\boldsymbol{n}_N + d_f\boldsymbol{n}_N)\ ds. \tag{34}$$

To further simplify the notation we define the translation operator $T_{\boldsymbol{\delta}}$ acting on any scalar or vector field $\xi(\boldsymbol{x})$,

$$T_{\boldsymbol{\delta}}\xi(\boldsymbol{x}) = \xi(\boldsymbol{x} + \boldsymbol{\delta}). \tag{35}$$

We also define a convolution operator $C_{\boldsymbol{n}}$ acting on any scalar or vector field as,

$$C_{\boldsymbol{n}}\mathbf{v}(\boldsymbol{x}) = \int_{-\infty}^{\infty} \varphi(s)\boldsymbol{n}\cdot\mathbf{v}(\boldsymbol{x}+\boldsymbol{n}s)\ ds. \tag{36}$$

For the North direction, Eq. (34) can be written as,

$$\tilde{v}_{rN} = C_{\boldsymbol{n}_N} T_{d_f \boldsymbol{n}_N}\mathbf{v}. \tag{37}$$

We get similar expressions for South, East and West directions. Eq. (32) can then be written as,

$$u_{wc} = \frac{1}{2\sin\phi}[(C_{\boldsymbol{n}_N}T_{d_f\boldsymbol{n}_N} - C_{\boldsymbol{n}_S}T_{d_f\boldsymbol{n}_S})\cos\Theta + (C_{\boldsymbol{n}_E}T_{d_f\boldsymbol{n}_E} - C_{\boldsymbol{n}_W}T_{d_f\boldsymbol{n}_W})\sin\Theta]\mathbf{v} \tag{38}$$

We also know that by definition,

$$\langle u'^2\rangle = \int \langle \hat{u}(\boldsymbol{k})\hat{u}^*(\boldsymbol{k})\rangle d\boldsymbol{k}, \tag{39}$$

where $\hat{}$ denotes Fourier transform and $*$ denotes complex conjugation. In the Fourier space we have,

$$\widehat{T_{\boldsymbol{\delta}}\mathbf{v}}(\boldsymbol{k}) = e^{\mathrm{i}\boldsymbol{k}\cdot\boldsymbol{\delta}}\hat{\mathbf{v}}(\boldsymbol{k}), \tag{40}$$

$$\widehat{C_{\boldsymbol{n}}\mathbf{v}}(\boldsymbol{k}) = \hat{\varphi}(\boldsymbol{n}\cdot\boldsymbol{k})\boldsymbol{n}\cdot\hat{\mathbf{v}}(\boldsymbol{k}), \tag{41}$$

where $\hat{\varphi}(k) = \mathrm{sinc}^2(kl_p/2)$, considering that the weighting function for a pulsed lidar is commonly defined as,

$$\varphi(s) = \begin{cases} \frac{l_p - |s|}{l_p^2} & \text{for } |s| < l_p; \\ 0 & \text{elsewhere,} \end{cases} \tag{42}$$

where l_p is the half length of the ideally rectangular light pulse leaving the lidar assuming the matching time windowing ($= 2l_p/c$, where c is the speed of light). Thus in Fourier space Eq. (38) can then be written as,

$$\begin{aligned} \hat{u}_{wc}(\boldsymbol{k}) =& \frac{1}{2\sin\phi}[(\boldsymbol{n}_N e^{\mathrm{i}d_f\boldsymbol{k}\cdot\boldsymbol{n}_N}\,\mathrm{sinc}^2(\boldsymbol{k}\cdot\boldsymbol{n}_N l_p/2) - \boldsymbol{n}_S e^{\mathrm{i}d_f\boldsymbol{k}\cdot\boldsymbol{n}_S}\,\mathrm{sinc}^2(\boldsymbol{k}\cdot\boldsymbol{n}_S l_p/2))\cos\Theta \\ &+ (\boldsymbol{n}_E e^{\mathrm{i}d_f\boldsymbol{k}\cdot\boldsymbol{n}_E}\,\mathrm{sinc}^2(\boldsymbol{k}\cdot\boldsymbol{n}_E l_p/2) - \boldsymbol{n}_W e^{\mathrm{i}d_f\boldsymbol{k}\cdot\boldsymbol{n}_W}\,\mathrm{sinc}^2(\boldsymbol{k}\cdot\boldsymbol{n}_W l_p/2))\sin\Theta]\cdot\hat{\mathbf{v}}(\boldsymbol{k}) \\ &\equiv \boldsymbol{b}(\boldsymbol{k})\cdot\hat{\mathbf{v}}(\boldsymbol{k}), \end{aligned} \tag{43}$$

and the variance (from Eq. 39),

$$\langle u_{wc}'^2\rangle = \int \Phi_{ij}(\boldsymbol{k})b_i(\boldsymbol{k})b_j^*(\boldsymbol{k})\ d\boldsymbol{k}, \tag{44}$$

where we have implicitly used the relation, $\Phi_{ij}(\boldsymbol{k}) = \langle\hat{\mathrm{v}}_i(\boldsymbol{k})\hat{\mathrm{v}}_j^*(\boldsymbol{k})\rangle$. The (co-) variances of other components can be estimated in a similar manner by first estimating the corresponding weighting functions $c_i(\boldsymbol{k})$ and $a_i(\boldsymbol{k})$ for v_{wc} and w_{wc} components respectively.

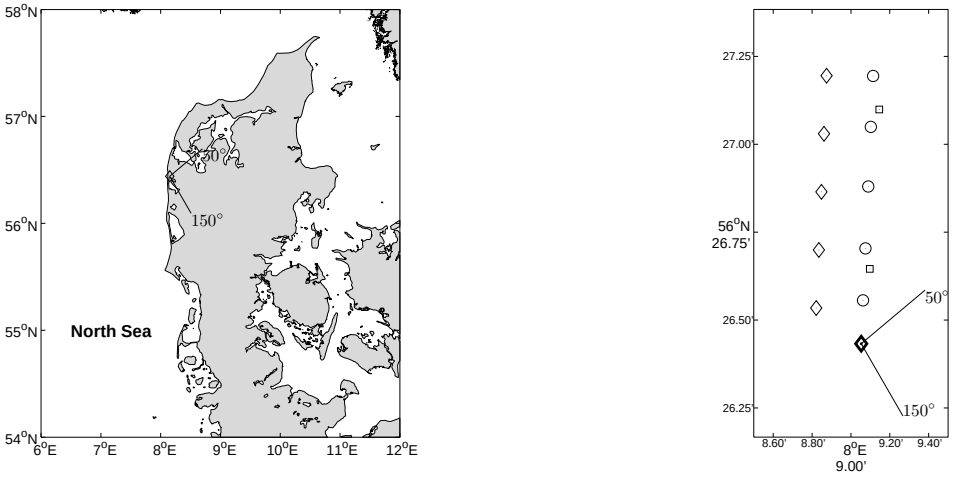

(a) (b)

Figure 2: Location of the Høvsøre met-mast and details of the site. The wind turbines are marked as circles, light tower as squares and the meteorological masts as diamonds. The meteorological mast from which the measurements are used is indicated as a dark diamond and the selected wind direction is also shown.

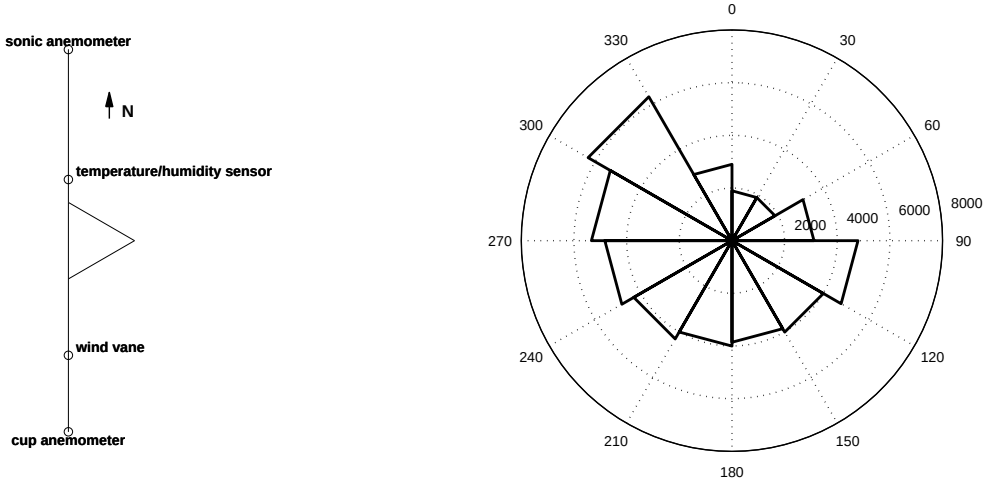

(a) Sensor Orientation (b) Wind Rose

Figure 3: Orientation of the sensors on the meteorological mast and wind rose at 60 m. The numbers inside the circles are the number of 10-min observations

2.1.3 Comparison of the model with the measurements

The measurements were performed at the Danish National Test Center for Large Wind Turbines at Høvsøre, Denmark. Figure 2 shows the layout of the test center and the location of the used reference meteorological (met.) mast, a 116.5 m tall intensively equipped mast located at the coordinates 56°26'26" N, 08°09'03" E, (indicated by a dark diamond in Fig. 2b). The site is about 2 km from the west coast of Denmark. The eastern sector is characterized by flat homogeneous terrain, and to the south is a lagoon.

Our reference measurements for this study are the sonic anemometer measurements taken at

40, 60, 80 and 100 m. The measured three-dimensional wind speeds are resolved with a frequency of 20 Hz and then reduced to the respective 10-min statistics (mean values and standard deviations or variances). All sonic anemometers are placed on the North booms of the met. mast (Fig. 3a), resulting in unusable data when the wind is from the south due to the wake of the mast. In combination with the sonic measurements, wind speeds from a ZephIR (coordinates 56°26'26.9556" N, 08°09'2.448" E) and a WindCube (coordinates 56°26'26.0556" N, 08°09'3.226" E) are used. The ZephIR is located about 35m North of the met. mast and the WindCube is located about 5m North-West of the met. mast. Reference and lidar data were collected over two different time periods, for the WindCube between January and April 2009, and for the ZephIR between April and November 2009. In order to further avoid the influence of the wakes from the wind turbines and the met. mast on lidar measurements, and inhomogeneities due to the sudden change of roughness (sea-land transition, see Fig. 2a), only data periods with easterly winds (50°–150°) are analyzed. Fig. 3b shows that although the dominant wind direction is West-North-West, there is also sufficient data in the chosen directional (eastern) sector. For the ZephIr 5530 data points were used after using all the filter, whereas for the WindCube 4003 data points were used.

The precision of the sonic anemometer measurements is estimated to be about ±1.5%. From comparisons with cup anemometers, the mean error of the WindCube in typical flat coastal conditions is within ±0.05 m/s with a standard deviation in mixed shear conditions of about 0.15 m/s. The corresponding uncertainty for the measurements made with a ZephIR is slightly higher (A detailed list of different error sources is given in Lindelöw-Marsden (2009)).

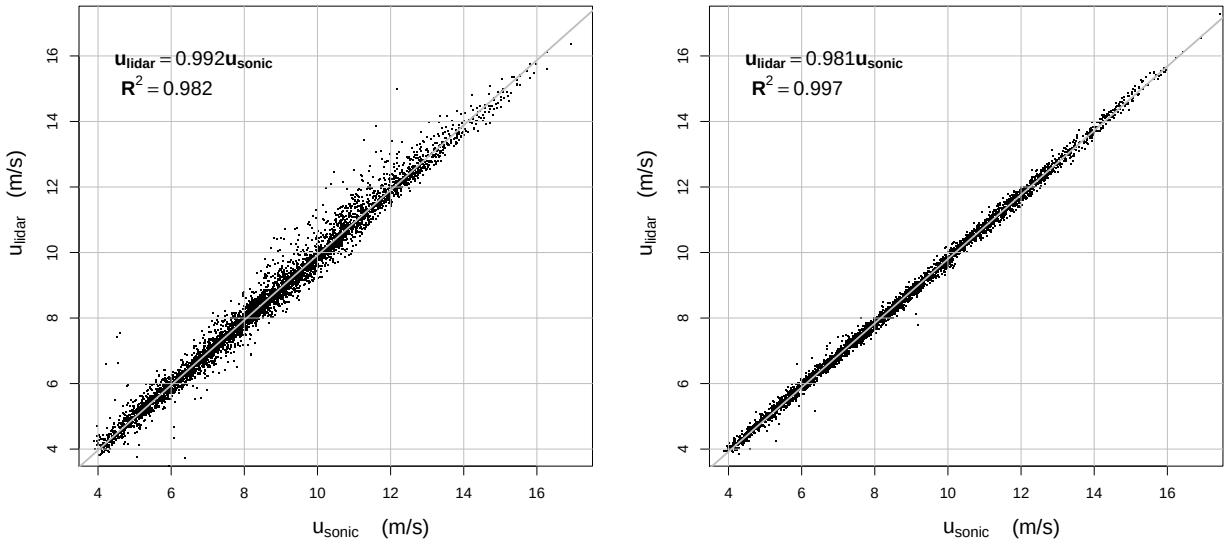

(a) ZephIR

(b) WindCube

Figure 4: Comparison of the mean wind speed measured by lidars and sonic anemometer

Fig. 4 shows the comparison of the 10-min mean horizontal wind speed (at 100 m) measured by the ZephIR and WindCube with the sonic anemometer. Data are shown for the easterly winds (50°–150°) and reference mean wind speeds between 4 m/s and 25 m/s. To guarantee repeatable conditions the data were furthermore filtered with respect to rain (i.e. only 10-min periods with no precipitation were considered) and the availability of the lidar (i.e. 100% of the fast data within a 10-min period had to be available). The lidar observations agree reasonably well with those of the sonic anemometer, with coefficients of determination $R^2 > 0.98$, where the data of the WindCube shows a significantly better correlation than those of the ZephIR. The estimation of Φ_{ij} using the

model from Mann (1994) requires three input parameters, $\alpha\epsilon^{2/3}$, which is a product of the spectral Kolmogorov constant α (Monin and Yaglom, 1975) and the rate of viscous dissipation of specific turbulent kinetic energy $\epsilon^{2/3}$, a length scale L and an anisotropy parameter Γ. We use these input parameters obtained by fitting the sonic anemometer measurements under different atmospheric stability conditions, at several heights on the meteorological mast in the eastern sector (Peña et al., 2010). The classification of atmospheric stability (table 1) is based on the Monin-Obukhov length (L_{MO}) intervals (Gryning et al., 2007).

Table 1: Classification of atmospheric stability according to Monin-Obukhov length intervals

very stable (vs)	$10 \leq L_{MO} \leq 50$ m
stable (s)	$50 \leq L_{MO} \leq 200$ m
near-neutral stable (nns)	$200 \leq L_{MO} \leq 500$ m
neutral (n)	$\mid L_{MO} \mid \geq 500$ m
near-neutral unstable (nnu)	$-500 \leq L_{MO} \leq -200$ m
unstable (u)	$-200 \leq L_{MO} \leq -100$ m
very unstable (vu)	$-100 \leq L_{MO} \leq -50$ m

L_{MO} is estimated using the eddy covariance method (Kaimal and Finnigan, 1994) from the high frequency (20 Hz) measurements at 20 m. Mathematically, L_{MO} is given as,

$$L_{MO} = -\frac{{u_*}^3 T}{\kappa g \overline{w'\theta'_v}}, \tag{45}$$

where u_* is the friction velocity, $\kappa = 0.4$ is the von Kármán constant, g is the acceleration due to gravity, T is the absolute temperature, θ_v is the virtual potential temperature and $\overline{w'\theta'_v}$ (covariance of w and θ_v)is the virtual kinematic heat flux. u_* is estimated as,

$$u_* = \sqrt[4]{\overline{u'w'}^2 + \overline{v'w'}^2}, \tag{46}$$

where $\overline{u'w'}$ (covariance of u and w) and $\overline{v'w'}$ (covariance of v and w) are the vertical fluxes of the horizontal momentum. For simplicity we define systematic error as the ratio of the lidar to the true second-order moment. Thus a ratio equal to one would signify no systematic error, whereas deviations from unity signify systematic error. By definition, the true second-order moment of a velocity component is given as,

$$\langle \mathrm{v}'_i \mathrm{v}'_j \rangle = \int \Phi_{ij}(\boldsymbol{k}) d\boldsymbol{k}. \tag{47}$$

The theoretical systematic errors are calculated by taking the ratio of lidar second-order moments (Eqs. 15, 18, 19 and 43) to the true second-order moment (Eqn. 47). The numerical integration is carried out using an adaptive algorithm (Genz and Malik, 1980). For experimental comparison, the second-order moments measured by sonic anemometers are considered to be true second-order moments. Thus experimentally, the systematic errors are estimated by taking the ratio of the measured lidar second-order moments to sonic second-order moments.

Fig. 5 shows the comparison of the modelled and measured systematic errors of u, v and w variances for the CW lidar over 10 minute periods. The theoretical points are shown with and without the low-pass filter. For the low-pass filter, the model is dependent on the mean wind speed and the plots are shown for $\langle u \rangle = 9$ m/s at all heights, since this is the mean wind speed at Høvsøre. The measurements are represented as median (markers), first and third quartiles (error bars) respectively. We infer the following:

- The systematic errors vary considerably under different atmospheric stability conditions – The variation is up to 50% for u and v variances, and up to 20% for w variance. This is due

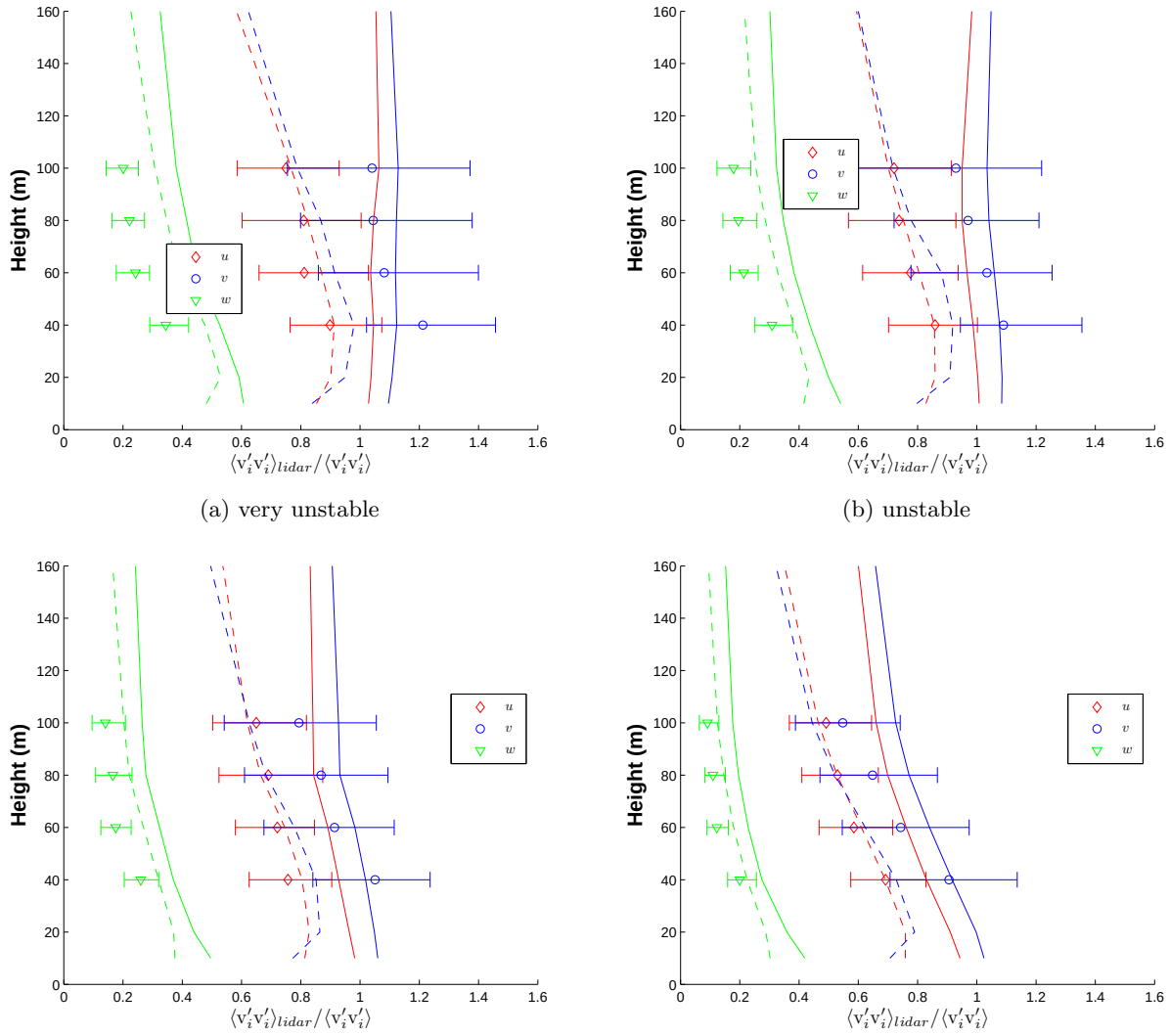

(a) very unstable

(b) unstable

(c) near neutral unstable

(d) neutral

Figure 5: ZephIR systematic errors under different atmospheric stability conditions in the eastern sector. The markers indicate measurements. The solid lines are the theory without the low-pass filter, and the dashed lines are with the low-pass filter.

to a large variation in the length scales of different velocity components resulting in varying attenuation of the variances.

- The systematic errors increase with height under all atmospheric stability conditions – This is due to a quadratic increase in the sample volume with height (Lindelöw, 2007). The diameter of the scanning circle also increases with height.

- The systematic errors in w variance are much larger (approximately 3-5 times) than that of the u and v variances – This is due to the very small length scales of the w component as compared to those for u and v, resulting in the attenuation of the w variance of up to 90%. The u and v variances are attenuated up to 70%.

- There is a significant spread (first and third quartiles) in the systematic errors of u and v variances – These are the random errors and most likely occur due to the disjunct sampling

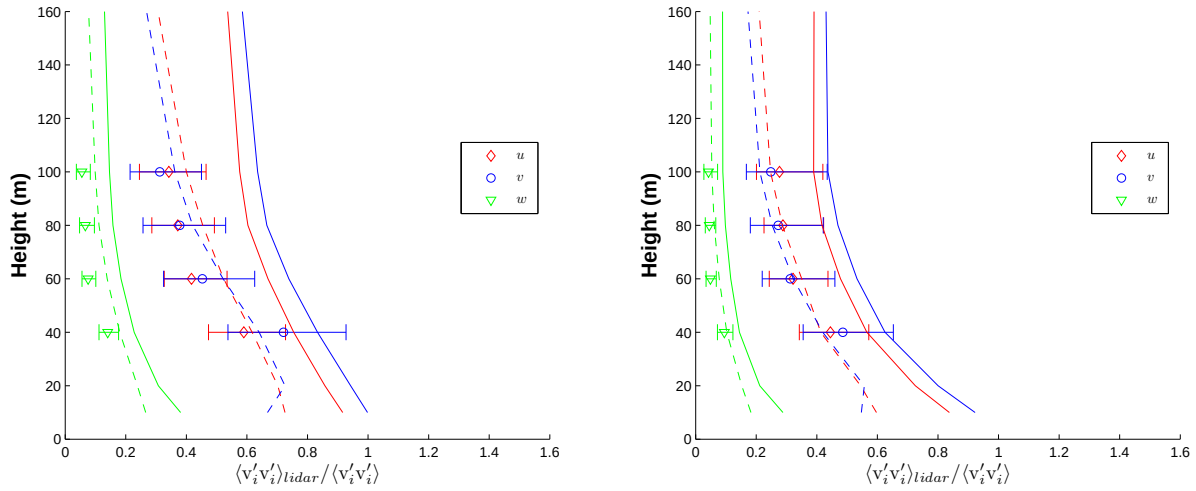

(e) near neutral stable

(f) stable

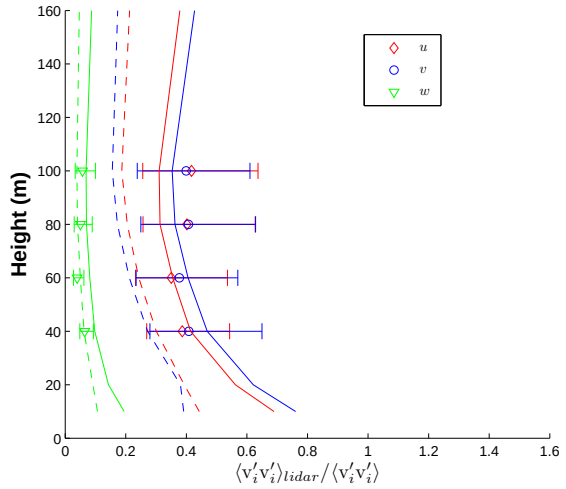

(g) very stable

Figure 5: ZephIR systematic errors under different atmospheric stability conditions in the eastern sector. The markers indicate measurements. The solid lines are the theory without the low-pass filter, and the dashed lines are with the low-pass filter.

(Lenschow et al., 1994) of the ZephIR. A thorough scientific investigation is needed to quantify random errors, but is not the focus of this paper.

- The trend of the systematic errors predicted by both models is in agreement with the observations at all heights.
- With the exception of very stable conditions, the model with the low-pass filter (Eqs. 24–26) is in better agreement with the measurements at all heights than without the low-pass filter.

In order to quantify the improvement in the model predictions using the low-pass filter, we compute the root mean square percent errors (RMSPE) between the measured and the modelled

systematic errors for each stability condition. RMSPE is given as,

$$RMSPE = \sqrt{\frac{\sum \left(\frac{\left(\frac{\langle v_i' v_i' \rangle_{lidar}}{\langle v_i' v_i' \rangle}\right)_{measured} - \left(\frac{\langle v_i' v_i' \rangle_{lidar}}{\langle v_i' v_i' \rangle}\right)_{modelled}}{\left(\frac{\langle v_i' v_i' \rangle_{lidar}}{\langle v_i' v_i' \rangle}\right)_{measured}} \times 100 \right)^2}{n}}, \tag{48}$$

where median values are used for the measurements.

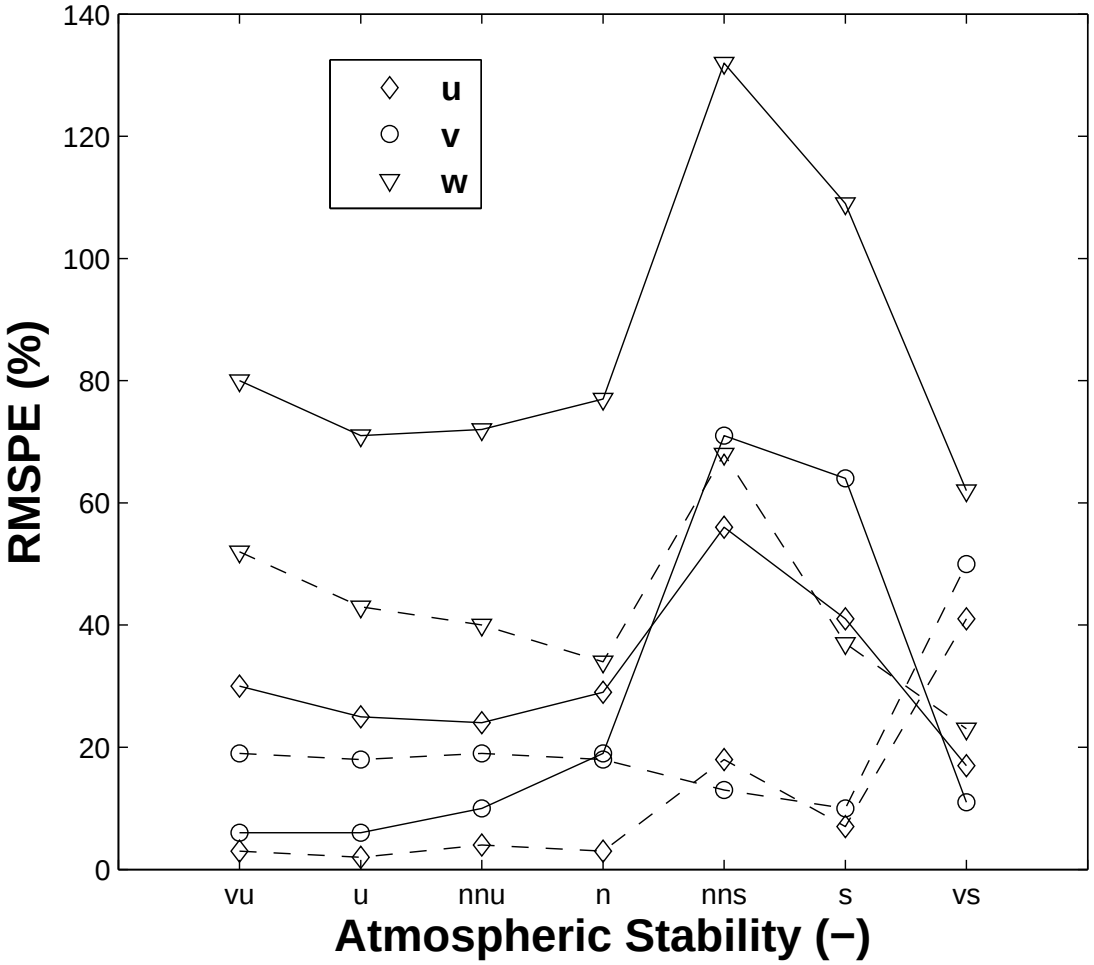

Figure 6: Root mean square percent error (RMSPE) in the prediction of the systematic errors for the ZephIR. The solid line shows the model without the low-pass filter and the dashed line shows the model with the low-pass filter. See table 1 for the meaning of the abbreviations on the x-axis.

Fig. 6 shows the comparison of the RMSPE in the prediction of the systematic errors with and without the low-pass filter for the ZephIR. A significant decrease in the RMSPE (of the order of 30%) of u and w variances is observed under all atmospheric stabilities (except for the very stable condition for u variance), when the low-pass filtering is used. For the v variance, there is a slight increase (up to 10%) in the RMSPE under unstable conditions, whereas for stable conditions a decrease of up to 40% is observed. Thus, in general, using the low-pass filter, the model predicts the systematic errors better than without using the low-pass filter. We also performed the calculations

using the beam radius $r_b = 24$ mm, and observed that the RMSPE for all three variance components changes only slightly ($\pm 5\%$).

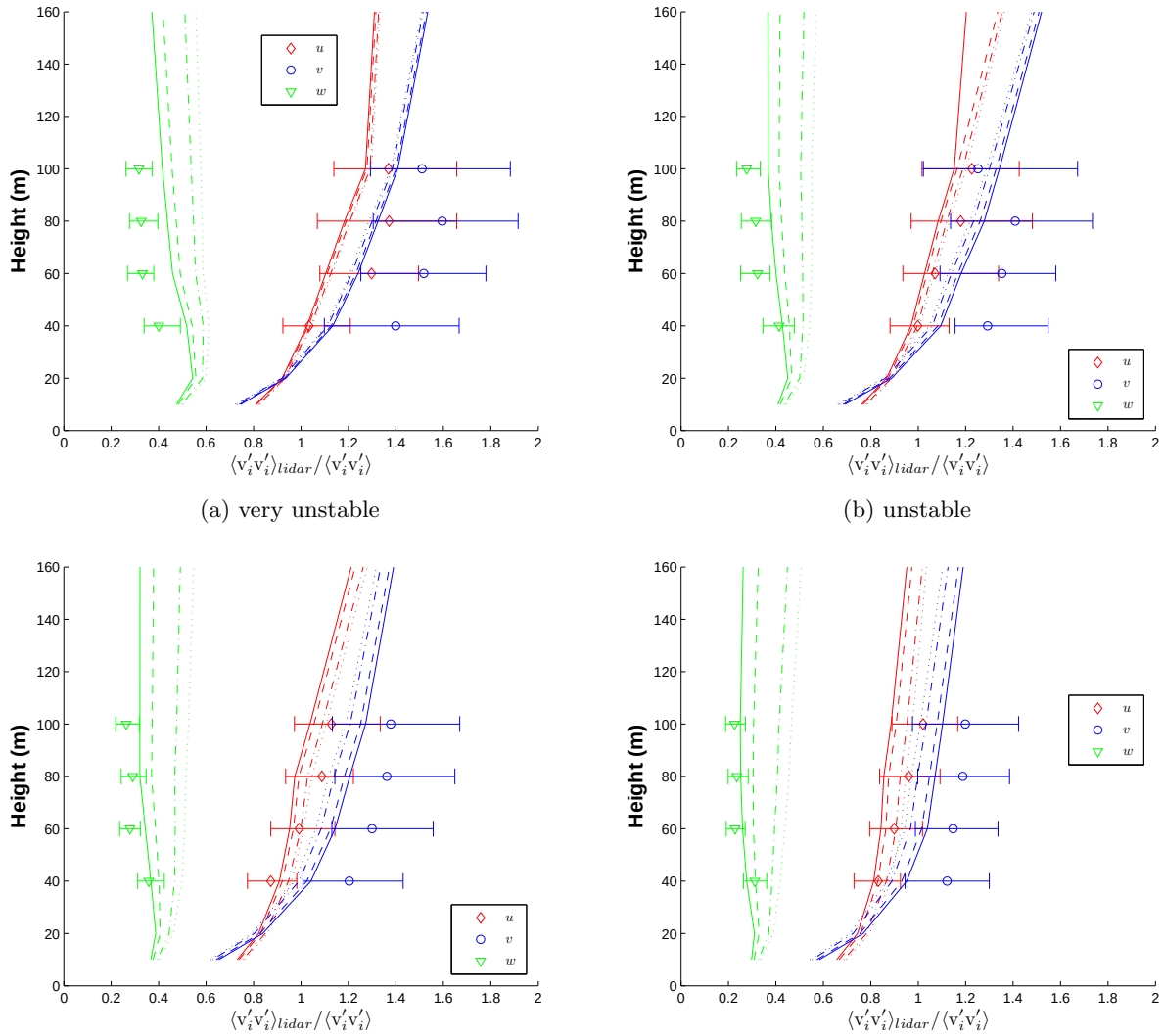

(a) very unstable

(b) unstable

(c) near neutral unstable

(d) neutral

Figure 7: WindCube systematic errors under different atmospheric stability conditions in the eastern sector. The markers indicate measurements. The model variation with wind direction is plotted as dotted line for 0°, dash-dot line for 15°, dashed line for 30° and solid line for 45°

Fig. 7 shows the comparison of the modelled and measured systematic errors of u, v and w variances for the pulsed lidar over 10-min periods. We infer the following:

- The systematic errors vary considerably under different atmospheric stability conditions – The variation is up to 50% for u and v variances, and up to 20% for the w variance. The same is also observed for the ZephIR.

- The systematic errors decrease with height for the u and v variances under all atmospheric stability conditions – For the WindCube, the probe length is constant (Lindelöw, 2007), and hence, at lower heights there is a combined averaging effect due to the probe length and the diameter of the scanning circle. Considering that at lower heights the length scales are smaller than at higher heights, it is likely that the variances are attenuated greater at lower heights

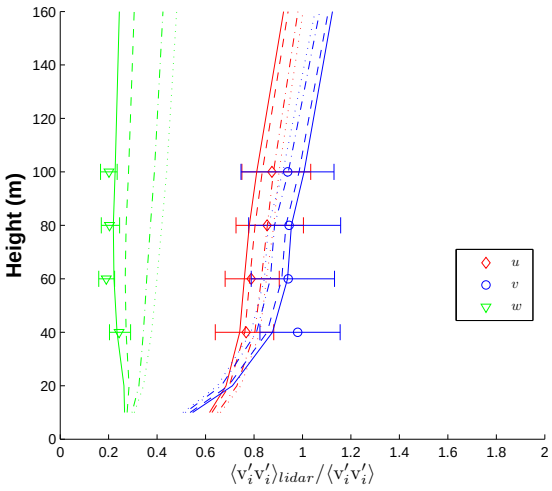

(e) near neutral stable

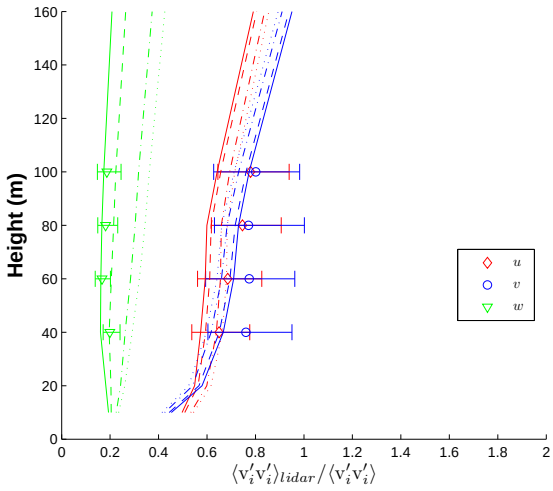

(f) stable

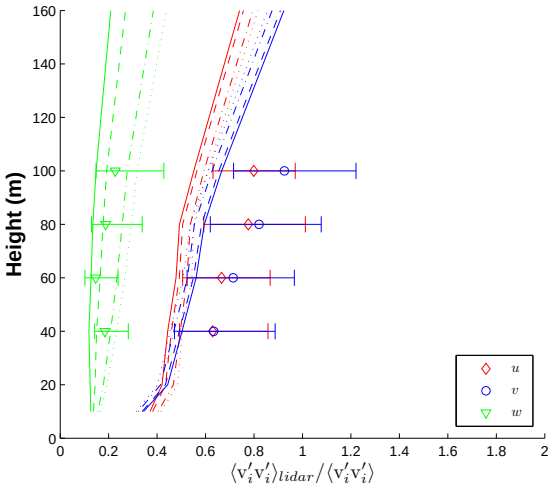

(g) very stable

Figure 7: WindCube systematic errors under different atmospheric stability conditions in the eastern sector. The markers indicate measurements. The model variation with wind direction is plotted as dotted line for 0°, dash-dot line for 15°, dashed line for 30° and solid line for 45°

than at higher heights. For w variance, the systematic error is approximately constant, and is most likely due to the small length scales.

- The systematic error in w variance is much larger (approximately 3-5 times) than that of the u and v variances. The same is also observed for the ZephIR.
- The spread in the systematic error (first and third quartiles) of the u and v variances is smaller than that of the ZephIR – This is most likely because the WindCube updates the velocity vector approximately every 6.5 seconds, whereas the ZephIR updates every 18 seconds.
- The systematic error varies significantly with the wind direction relative to the beam direction for w variance, and to a lesser degree for u and v variance under all stability conditions.

Fig. 8 shows the comparison of the RMSPE in the prediction of the systematic errors for the WindCube and ZephIR (with the low-pass filter). It is observed that for u and v variances, with

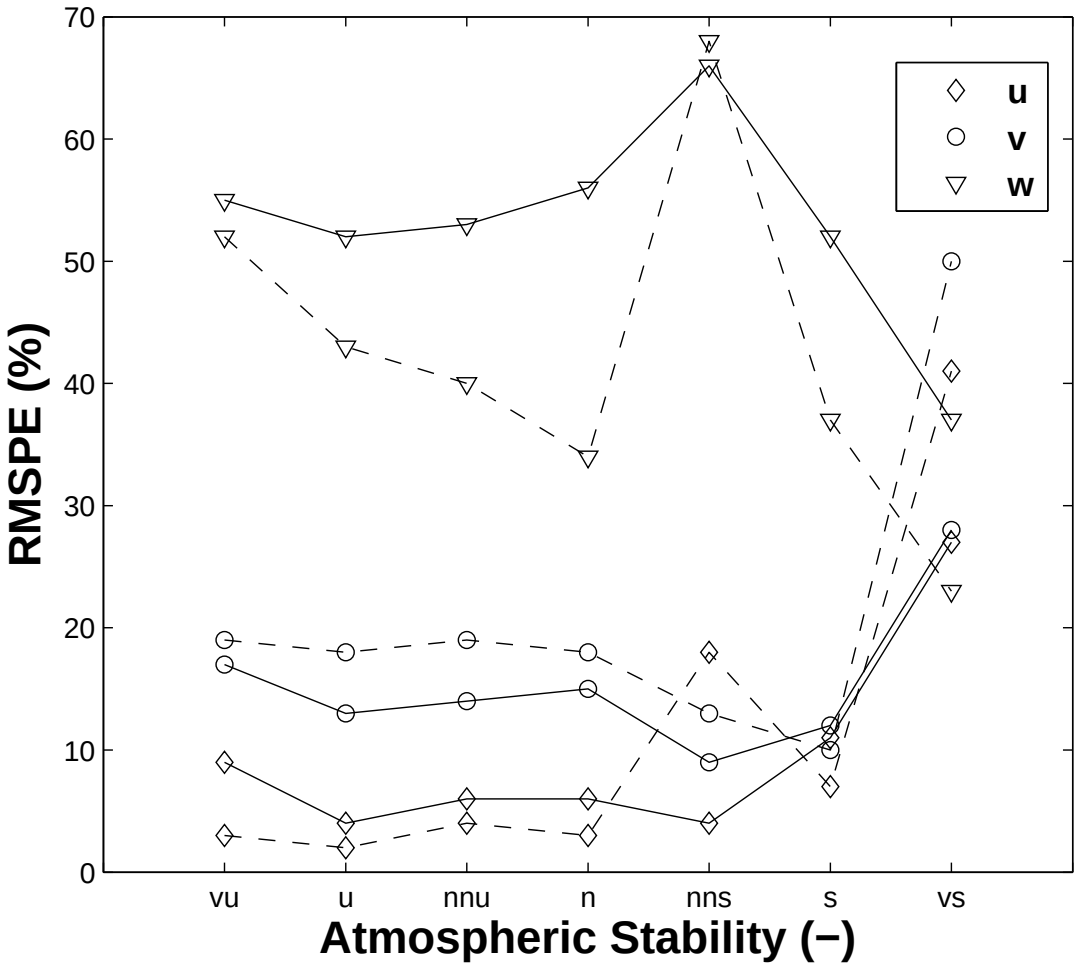

Figure 8: Comparison of the root mean square percent error (RMSPE) in the prediction of the systematic errors for the WindCube and ZephIR. The solid line is for the WindCube and the dashed line is for the ZephIR with the low-pass filter. See table 1 for the meaning of the abbreviations on the x-axis.

the exception of the near-neutral stable condition, the RMSPE in both lidars is approximately equal. There is a considerable variation in the RMSPE for the w variance. This is most likely because for the WindCube, the w variance is very sensitive to the wind direction due to its cosine and sine dependence. In general, for both lidars, except for the very stable condition, the model predicts the systematic errors for u variance reasonably well (RMSPE $\approx 6\%$), followed by v variance (RMSPE $\approx 12\%$). It is difficult to say whether the prediction for the w variance is less reliable or not (RMSPE of the order of 60%).

We do not model the filtering effect due to the scanning time (≈ 6.5 seconds) of WindCube for two reasons:

1. Since the measurement is carried out at only four points, each lasting 0.5 seconds on the scanning circle, we cannot assume that the WindCube measures infinitely fast on the scanning circle (as we did for the ZephIR). The translations in each direction have to be convolved with the corresponding spectral transfer function, if the filtering is to be included.

2. The calculation becomes too cumbersome if the above procedure is followed.

While comparing the performance of our model, the following should also be considered:

- The model is dependent on the three dimensional spectral velocity tensor (Mann, 1994), which is strictly valid for neutral conditions only. Thus, one has to be careful while comparing under different atmospheric stability conditions. In this study, we have reduced the uncertainty by using the the three input tensor parameters that are fitted to the measurements under different atmospheric stability conditions (Peña et al., 2010).

- While using Eqs. (24)–(26), we have used the same mean wind speed at all heights. In reality, there is always wind shear, which also depends significantly on atmospheric stability (Motta and Barthelmie, 2005). However, the calculations will become too cumbersome, and hence, we made a crude approximation.

- The very stable conditions are generally difficult to analyze. There could be different reasons for the large deviation in the u and v variances, e.g.,

  – Uncertainty in the input tensor parameters
  – Lack of validity of the spectral tensor model (Mann, 1994) under different atmospheric stability conditions

  Also, contrary to expectation, the measurements under very stable conditions (Figs. 5 and 7) show a decrease in the systematic errors for the u and v variances, as compared to the stable conditions.

There is also some room for reducing redundancy in the ZephIR measurements, which might reduce the spread of the systematic errors (quartile range). Instead of scanning at several points on the circle, only four points are required. Reducing the measurement points would increase the dependence of the second-order moments on the wind direction (refer section 2.1.2). However, it would considerably reduce the time required for completing a VAD. There is also no need to scan the circle three times, e.g. in the present configuration, 50 points are scanned in approximately one second. Thus four points would take only 0.08 seconds. If it measures five heights sequentially, the next measurement would be after 0.4 seconds, giving a measurement frequency > 2 Hz. Alternatively, at each of the four points the scans can also be performed rapidly at different heights sequentially before scanning the next point.

2.2 Turbulence spectra measurements

In this section the aim is to explain how a scanning pulsed wind lidar measures turbulence spectra in combination with the velocity azimuth display (VAD) technique of data processing. In particular, a theoretical model of the turbulence spectra measured by a pulsed wind lidar (WindCube) operating in a VAD mode is developed. The model is verified by comparing measurements from a lidar and a sonic anemometer (sonic). Similar to section 2.1 we first model the turbulence spectra as measured by the pulsed lidar and then compare our model with the measurements.

2.2.1 Modelling

By definition, the one-dimensional spectrum of any component of the wind field is given as (Wyngaard, 2010)

$$\begin{aligned} F_{ij}(k_1) &= \frac{1}{2\pi}\int_{-\infty}^{\infty} R_{ij}(x)\exp(-\mathrm{i}k_1 x)\, dx, \\ &= \frac{1}{2\pi}\lim_{X\to\infty}\int_{-X}^{X} R_{ij}(x)\exp(-\mathrm{i}k_1 x)\left(\frac{1-|x|}{X}\right) dx, \end{aligned} \tag{49}$$

where k_1 is the wavenumber, $F_{ij}(k_1)$ is the one-dimensional spectrum, $R_{ij}(x)$ is the autocovariance function, x is the separation distance, and X is the length of the record. Since the WindCube cannot make continuous measurements, let us take only discrete values such that $X = N\Delta x$ and $x = n\Delta x$, where n is an integer multiple, N is the total number of samples, and Δx is the distance traveled by the wind when the lidar beam shifts from one azimuth angle to the other. Since it takes about 4 s for the WindCube beam to move from the North to the South, or from the East to the West, assuming Taylor's hypothesis to be valid, we get $\Delta x = \bar{u} \times 4$ m, where $\bar{u}$ is the mean wind speed. If we evaluate the spectra measured by the WindCube at only discrete wave numbers $k_{1_q} = 2\pi q/X$, then we can write

$$F_{ij_{wc}}(q) = \frac{1}{2\pi} \sum_{n=-N}^{N} R_{ij_{wc}}(n) \exp\left(\frac{-\mathrm{i}2\pi nq}{N}\right)\left(1 - \frac{|n|}{N}\right)\ \Delta x. \tag{50}$$

The challenge now is to find an expression for $R_{ij_{wc}}(n)$. We first demonstrate the model of $R_{ij_{wc}}(n)$ for the u component and use the same framework to derive the v and w components.

We begin by considering the mathematical form of Taylor's hypothesis such that

$$\mathbf{v}(x,t) = \mathbf{v}(x - \Delta x, 0), \tag{51}$$

where t is the time. For simplicity, let us first neglect the averaging along the line-of-sight. We will introduce this averaging later in the equations. For the turbulence spectra measured by the WindCube, it is necessary to consider the exact spatial and temporal position of the measurements. The wind vector is constructed using the North and South beams such that at any given instant, one current and one previous measurement is used. If we assume that at $t = 0$, we use the current measurement from the North beam and the previous measurement from the South beam, then combining Eqs. (**??**) and (51) we can write

$$u_{wc}(m\Delta x) = \frac{\tilde{v}_{rS}(\boldsymbol{n}_S d_f - \boldsymbol{e}_1(m-1)\Delta x) - \tilde{v}_{rN}(\boldsymbol{n}_N d_f - \boldsymbol{e}_1 m\Delta x)}{2\sin\phi},\ \text{for even } m, \tag{52}$$

$$u_{wc}(m\Delta x) = \frac{\tilde{v}_{rS}(\boldsymbol{n}_S d_f - \boldsymbol{e}_1 m\Delta x) - \tilde{v}_{rN}(\boldsymbol{n}_N d_f - \boldsymbol{e}_1(m-1)\Delta x)}{2\sin\phi},\ \text{for odd } m, \tag{53}$$

where $\boldsymbol{e}_1 = (1,0,0)$ is the unit vector in the mean wind direction. Combining even and odd m from Eqs. (52) and (53), we can write

$$\begin{aligned} u_{wc}(m\Delta x) = &\Big[\tilde{v}_{rS}\Big(\boldsymbol{n}_S d_f - \boldsymbol{e}_1\big(m - \frac{(1+(-1)^m)}{2}\big)\Delta x\Big) \\ &- \tilde{v}_{rN}\Big(\boldsymbol{n}_N d_f - \boldsymbol{e}_1\big(m - \frac{(1-(-1)^m)}{2}\big)\Delta x\Big)\Big] \Big/ \Big(2\sin\phi\Big). \end{aligned} \tag{54}$$

We know that by definition, $R_{ij}(n) = \langle u_i(m\Delta x) u_j\big((m+n)\Delta x\big)\rangle$, where $\langle\rangle$ denotes ensemble averaging. By applying this definition to Eq. (54), we get auto and cross covariances for the North and South beams. Introducing the averaging along the beam (using Eq. 4) for only the south beam, we get

$$\begin{aligned} &\Big\langle \tilde{v}_{rS}\Big(\boldsymbol{n}_S d_f - \boldsymbol{e}_1\big(m - \frac{(1+(-1)^m)}{2}\big)\Delta x\Big)\tilde{v}_{rS}\Big(\boldsymbol{n}_S d_f - \boldsymbol{e}_1\big((m+n) - \frac{(1+(-1)^{m+n})}{2}\big)\Delta x\Big)\Big\rangle \\ &= \int_{-\infty}^{\infty}\int_{-\infty}^{\infty} n_{iS} n_{jS}\ \varphi(s_1)\varphi(s_2) \\ &\Big\langle \mathrm{v}_i\Big(\boldsymbol{n}_S d_f - \boldsymbol{e}_1\big(m - \frac{(1+(-1)^m)}{2}\big)\Delta x + \boldsymbol{n}_S s_1\Big) \\ &\mathrm{v}_j\Big(\boldsymbol{n}_S d_f - \boldsymbol{e}_1\big((m+n) - \frac{(1+(-1)^{m+n})}{2}\big)\Delta x + \boldsymbol{n}_S s_2\Big)\Big\rangle\ ds_1 ds_2 \end{aligned} \tag{55}$$

If we denote $\boldsymbol{r} = \Big(\boldsymbol{n}_S d_f - \boldsymbol{e}_1\big(m-(1+(-1)^m)/2\big)\Delta x\Big) - \Big(\boldsymbol{n}_S d_f - \boldsymbol{e}_1\big((m+n)-(1+(-1)^{m+n})/2\big)\Delta x\Big)$ as the separation distance between the S-S beam combination, then we can write

$$R_{\tilde{v}_{rS}}(n) = \int_{-\infty}^{\infty}\int_{-\infty}^{\infty} n_{iS}n_{jS}\ \varphi(s_1)\varphi(s_2)R_{ij}(\boldsymbol{r} + \boldsymbol{n}_S(s_1 - s_2))\ ds_1 ds_2, \tag{56}$$

where $R_{\tilde{v}_{rS}}(n)$ is the autocovariance of the radial velocity for the South beam. $R_{ij}(\boldsymbol{r})$ is related to the three dimensional spectral velocity tensor $\Phi_{ij}(\boldsymbol{k})$ by the inverse Fourier transform (Wyngaard, 2010), i.e.,

$$R_{ij}(\boldsymbol{r} + \boldsymbol{n}_S(s_1 - s_2)) = \int \Phi_{ij}(\boldsymbol{k}) \exp(\mathrm{i}\boldsymbol{k}\cdot(\boldsymbol{r} + \boldsymbol{n}_S(s_1 - s_2)))\ d\boldsymbol{k}, \tag{57}$$

where $\int d\boldsymbol{k} \equiv \int_{-\infty}^{\infty}\int_{-\infty}^{\infty}\int_{-\infty}^{\infty} dk_1 dk_2 dk_3$ and $\boldsymbol{k} = (k_1, k_2, k_3)$ denotes the wave vector. Substituting Eq. (57) into (56) and rearranging the terms, we get

$$R_{\tilde{v}_{rS}}(\boldsymbol{r}) = \int \Phi_{ij}(\boldsymbol{k})\ n_{iS}n_{jS}\ \exp(\mathrm{i}\boldsymbol{k}\cdot\boldsymbol{r})\ \hat{\varphi}(\boldsymbol{k}\cdot\boldsymbol{n}_S)\hat{\varphi}^*(\boldsymbol{k}\cdot\boldsymbol{n}_S)\ d\boldsymbol{k} \tag{58}$$

where $\hat{}$ denotes Fourier transform and * complex conjugation. Reducing the expression of $\boldsymbol{r}$, we get

$$\boldsymbol{r} = \boldsymbol{e}_1\Big((-1)^m\frac{\Delta x}{2}(1-(-1)^n) + n\Delta x\Big). \tag{59}$$

Similarly, if we assume that at $t = 0$ we use the current measurement from the South beam and the previous measurement from the North beam, then we get

$$\begin{aligned} u_{wc}(m\Delta x) = &\Big[\tilde{v}_{rS}\Big(\boldsymbol{n}_S d_f - \boldsymbol{e}_1\big(m - \frac{(1-(-1)^m)}{2}\big)\Delta x\Big) \\ &- \tilde{v}_{rN}\Big(\boldsymbol{n}_N d_f - \boldsymbol{e}_1\big(m - \frac{(1+(-1)^m)}{2}\big)\Delta x\Big)\Big] \Big/ \Big(2\sin\phi\Big), \end{aligned} \tag{60}$$

and the separation distance for the S-S beam combination is given as $\boldsymbol{r} = -(-1)^m\Delta x/2(1-(-1)^n) + n\Delta x$. In order to make the time series statistically stationary, we consider that there is an equal probability that the beam at $t = 0$ points either in the North or South direction. This eliminates the dependence of the autocovariance function on m. We perform similar analysis on the auto and cross covariances for other beams. In total, we then get eight separation distances; two for the S-S, two for S-N, two for N-S, and two for N-N beam combinations. If we denote $\boldsymbol{r}_{u_l}$ (the subscript l denotes the respective beam combination) as the separation distance for different beam combinations, then we can write all the separation distances in compact form as

$$\boldsymbol{r}_{u_l} = \begin{cases} \boldsymbol{e}_1\Big((-1)^l\frac{\Delta x}{2}(1-(-1)^n) + n\Delta x\Big) & \text{for } l = 1,2,7,8; \\ \boldsymbol{n}_S d_f - \boldsymbol{n}_N d_f + \boldsymbol{e}_1\Big((-1)^l\frac{\Delta x}{2}(1+(-1)^n) + n\Delta x\Big) & \text{for } l = 3,4; \\ \boldsymbol{n}_N d_f - \boldsymbol{n}_S d_f + \boldsymbol{e}_1\Big((-1)^l\frac{\Delta x}{2}(1+(-1)^n) + n\Delta x\Big) & \text{for } l = 5,6. \end{cases} \tag{61}$$

Following a similar procedure for the v component, we get the following separation distances:

$$\boldsymbol{r}_{v_l} = \begin{cases} \boldsymbol{e}_1\Big((-1)^l\frac{\Delta x}{2}(1-(-1)^n) + n\Delta x\Big) & \text{for } l = 1,2,7,8; \\ \boldsymbol{n}_E d_f - \boldsymbol{n}_W d_f + \boldsymbol{e}_1\Big((-1)^l\frac{\Delta x}{2}(1+(-1)^n) + n\Delta x\Big) & \text{for } l = 3,4; \\ \boldsymbol{n}_W d_f - \boldsymbol{n}_E d_f + \boldsymbol{e}_1\Big((-1)^l\frac{\Delta x}{2}(1+(-1)^n) + n\Delta x\Big) & \text{for } l = 5,6. \end{cases} \tag{62}$$

The separation distances for the w component are the same as those for the u component, because only the North and South beams are used to obtain w_{wc} (Eq. 31). Combining Eqs. (52)–(62) and

using the symmetry properties of $\Phi_{ij}(\boldsymbol{k})$, we get the expressions for the autocovariance of the u and v components as

$$R_{u_{wc}}(n) = \frac{1}{8\sin^2\phi}\int \Phi_{ij}(\boldsymbol{k})\Big[n_{iS}n_{jS}\hat{\varphi}(\boldsymbol{k}\cdot\boldsymbol{n}_S)\hat{\varphi}^*(\boldsymbol{k}\cdot\boldsymbol{n}_S)\sum_{l=1}^{2}\exp(\mathrm{i}\boldsymbol{k}\cdot\boldsymbol{r}_{u_l}) - n_{iS}n_{jN}\hat{\varphi}(\boldsymbol{k}\cdot\boldsymbol{n}_S)\hat{\varphi}^*(\boldsymbol{k}\cdot\boldsymbol{n}_N)\sum_{l=3}^{6}\exp(\mathrm{i}\boldsymbol{k}\cdot\boldsymbol{r}_{u_l}) + n_{iN}n_{jN}\hat{\varphi}(\boldsymbol{k}\cdot\boldsymbol{n}_N)\hat{\varphi}^*(\boldsymbol{k}\cdot\boldsymbol{n}_N)\sum_{l=7}^{8}\exp(\mathrm{i}\boldsymbol{k}\cdot\boldsymbol{r}_{u_l})\Big]d\boldsymbol{k}, \tag{63}$$

$$R_{v_{wc}}(n) = \frac{1}{8\sin^2\phi}\int \Phi_{ij}(\boldsymbol{k})\Big[n_{iE}n_{jE}\hat{\varphi}(\boldsymbol{k}\cdot\boldsymbol{n}_E)\hat{\varphi}^*(\boldsymbol{k}\cdot\boldsymbol{n}_E)\sum_{l=1}^{2}\exp(\mathrm{i}\boldsymbol{k}\cdot\boldsymbol{r}_{v_l}) - n_{iE}n_{jW}\hat{\varphi}(\boldsymbol{k}\cdot\boldsymbol{n}_E)\hat{\varphi}^*(\boldsymbol{k}\cdot\boldsymbol{n}_W)\sum_{l=3}^{6}\exp(\mathrm{i}\boldsymbol{k}\cdot\boldsymbol{r}_{v_l}) + n_{iW}n_{jW}\hat{\varphi}(\boldsymbol{k}\cdot\boldsymbol{n}_W)\hat{\varphi}^*(\boldsymbol{k}\cdot\boldsymbol{n}_W)\sum_{l=7}^{8}\exp(\mathrm{i}\boldsymbol{k}\cdot\boldsymbol{r}_{v_l})\Big]d\boldsymbol{k}. \tag{64}$$

The expression for the w component is similar to that for the u component, except that the second term in the square brackets of Eq. (63) is added instead of subtracted, and $\sin^2\phi$ is replaced by $\cos^2\phi$ in the denominator. Substituting Eqs. (63) and (64) into Eq. (50), we can finally theoretically calculate the turbulence spectra measured by the WindCube for the u, v, and w components of the velocity field.

In order to see the extent of attenuation and redistribution of the spectral energy, we compare these models with the true theoretical spectra measured by sonics and those measured by the WindCube. The true theoretical spectrum of any component of the wind field is also given as (apart from Eq. 49) (Wyngaard, 2010),

$$F_{ij}(k_1) = \int_{-\infty}^{\infty}\int_{-\infty}^{\infty}\Phi_{ij}(\boldsymbol{k})\; dk_2 dk_3. \tag{65}$$

We consider the sonic measurements to essentially represent the true theoretical spectra.

2.2.2 Comparison with the measurements

The measurements are taken from the site described in section 2.1.3. We use the Metek USA-1 sonic measurements at 60 and 100 m in combination with the WindCube ($\approx$ 30 m range resolution) to compare with the modeled turbulence spectra. The WindCube is located about 5 m North-West of the met-mast, and the data were collected between January and April 2009. In order to avoid interference with the met-mast, the WindCube is turned in a horizontal plane such that the nominal North beam is 45° (i.e., in a North-East direction) with respect to true North. The frequency of measurement for the sonics is 20 Hz, whereas the WindCube takes approximately 2 s to shift from one azimuth angle to the other. We use the measurements from a narrow directional sector of 130°–140° only in order to align the mean wind direction with the nominal E-W beam of the WindCube. Thus, the u and w component measurements are deduced from the nominal E-W beams and the v component measurements are deduced from the nominal N-S beams.

The other criteria for the selection of the data are neutral atmospheric stability and a mean wind speed of 9 m/s. This wind speed was chosen because the Mann (1994) model parameters were available at 9 m/s. Using Taylor's hypothesis, we then have the sampling distance in the mean

wind direction $\Delta x = 9 \times 4$ m. We selected the data with a mean wind speed in the interval 8-10 m/s, which resulted in 79 and 58 10-min time series of the sonics and the WindCube at 60 and 100 m, respectively. Atmospheric stability is characterized using the standard surface-layer length scale L_{MO}, commonly known as the Monin-Obukhov length. Following Gryning et al. (2007), the conditions are considered neutral when $|L_{MO}| > 500$. L_{MO} is estimated using the eddy covariance method (Kaimal and Finnigan, 1994) from the sonic measurements at 20 m.

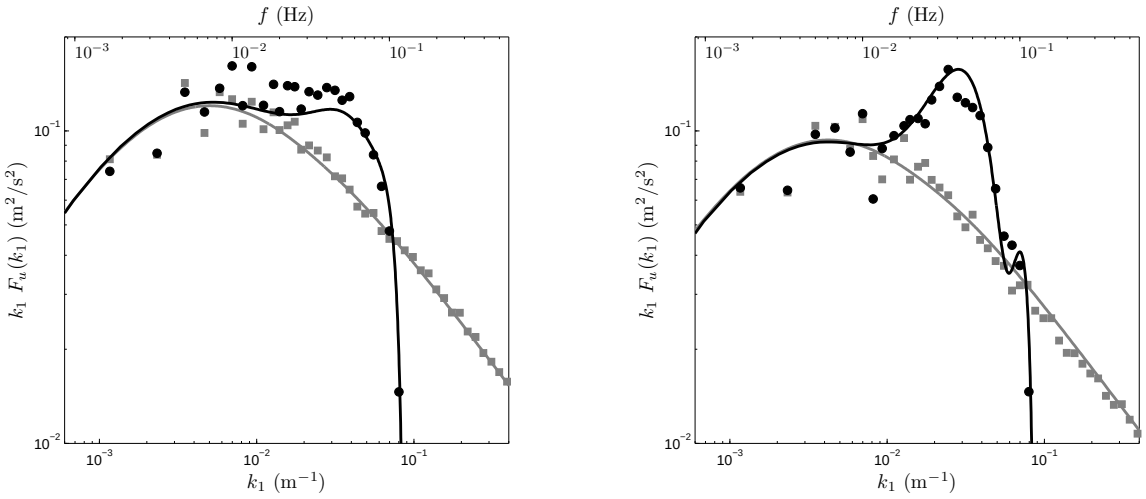

Figure 9: Comparison of the modeled and measured u spectrum at 60 m (left) and 100 m (right). The markers indicate measurements and the continuous line indicates the model. The black and gray markers denote WindCube spectrum and sonic spectrum, respectively.

Fig. 9 shows the comparison of the modeled and measured u spectrum at 60 and 100 m. The measurements indicate that the spectrum measured by the WindCube deviates significantly from the standard surface-layer spectrum as the turbulence scales decrease approximately from $k_1 > 0.005$ m^{-1}. Approximately in the inertial sub-range, where the sonic spectra scales with $k_1^{-5/3}$, there is an almost complete attenuation of the turbulence signal, and hence a rapid decrease in the spectral energy. This observation has a striking resemblance with that of Canadillas et al. (2010), where an independent measurement under neutral conditions in the German North Sea showed an increase in the spectral energy above $k_1 > 0.005$ m^{-1} and subsequent rapid attenuation. One of the reasons for this redistribution of the spectral energy is the contribution of the auto and cross covariances of different components of the velocity field, as seen in Eq. (63). At very low wavenumbers (< 0.005 m^{-1}), the spectral energy measured by the WindCube is approximately the same as that measured by the sonics. This is because very large turbulence eddies are associated with very low wavenumbers that cause the volume measurement from the lidar to behave essentially like a point measurement.

At both heights, our model agrees very well with the measurements at almost all wavenumbers. The point-like behavior of the WindCube at very low wavenumbers, and redistribution of the spectral energy beyond $k_1 > 0.005$ m^{-1}, is captured by the model very well. However, there are stark differences in the distribution of the spectral energy at 60 and 100 m. This is because of the beam interference phenomenon that occurs for certain separation distances at 100 m. This is explained as follows.

In our model, we have assumed validity of Taylor's hypothesis, which states that turbulence is advected by the mean wind field, i.e., the local velocity of the turbulent eddies is so small that they essentially move with only the mean velocity. In other words, turbulence can be considered to be frozen. For the u spectrum, we use only the N-S beams that are aligned in the mean wind

direction. At 100 m, the mean wind speed is such that the North and South beams will investigate the same air (but different components) after approximately $3\Delta x$. Looking more closely at Eq. (61), at $3\Delta x$ we get $r_{u_3} \to 0$ and $r_{u_4} \to 0$. This implies that in Eq. (63), $\exp(\mathrm{i}\boldsymbol{k} \cdot r_{u_3}) \to 1$ and $\exp(\mathrm{i}\boldsymbol{k} \cdot r_{u_4}) \to 1$. This will cause an overall decrease in $R_{u_{wc}}(n)$ at $n = 3$. From our calculations, we also find anomalous behavior of $R_{u_{wc}}(n)$ at $n = 2$ and $n = 4$. Revisiting Eq. (61), we find that at $n = 2$, $r_{u_3} \to 0$ and at $n = 4$, $r_{u_4} \to 0$. This implies that it will cause some reduction in $R_{u_{wc}}(n)$, but not as much as when $n = 3$. In order to explain this behavior, we illustrate the interference phenomenon of the beams in Fig. 10.

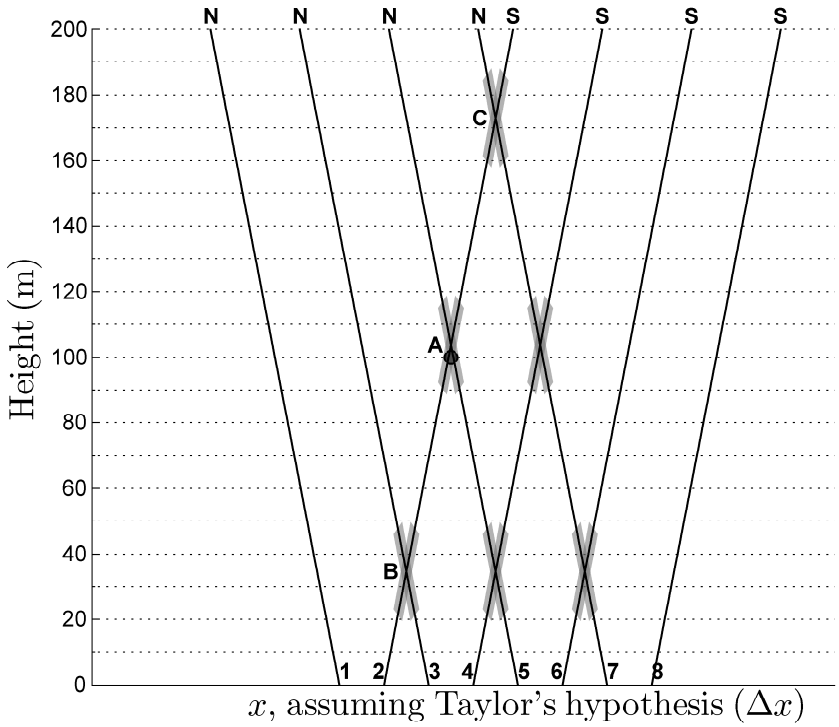

Figure 10: Schematic of the intersection of the North and South Beams. The shaded portion indicates the measurement volume. The black marker indicates a height of 100 m

Since we assume Taylor's hypothesis, we can either fix the N-S beams and measure the flow field as it moves past the beams, or freeze the flow field and move the N-S beams instead. For simplicity, let us freeze the flow field and represent 1–8 as the positions at which the North and the South beams perform measurements. The difference between each position is then equal to the separation distance Δx. Let 1, 3, 5, and 7 denote the measurements of the North beam and 2, 4, 6, and 8 denote those of the South beam. For now, let us consider only the intersection of beams 2 and 5 at point A, which is the point where the North and South beams will see the same air. This occurs at a separation distance of $3\Delta x$ corresponding to a height of 104 m. As a result, we will get unusual covariances whenever there is intersection of beams 2 and 5 in combination with other beam measurements. Since the WindCube uses one current and one previous measurement to deduce wind field components, we use the measurement from beam 2 when it is in combination with beam 1 or 3. Similarly, we use beam 5 when it is in combination with beam 4 or 6. These combinations can be written as

$$\begin{bmatrix} (\mathbf{2}, 1) & (\mathbf{3}, 2) \\ (\mathbf{5}, 4) & (\mathbf{6}, 5) \end{bmatrix} \tag{66}$$

The bold numbers in Eq. (66) indicate the current measurement for the respective beams, i.e., the set $(\mathbf{2}, 1)$ indicates that the current measurement from beam 2 is used in combination with the previous measurement from beam 1 to deduce the u component, and so on for other sets. In this case, we will obtain unusual covariances at these separation distances in the model, which are equal to the difference between beam numbers in bold (Eq. 66) that correspond to the intersection of beams 2 and 5. This happens at $\mathbf{5}-\mathbf{3}$, $\mathbf{5}-\mathbf{2}$, and $\mathbf{6}-\mathbf{2}$, corresponding to separation distances of $2\Delta x$, $3\Delta x$, and $4\Delta x$, respectively. We do not get unusual covariances at $\mathbf{3}-\mathbf{2}$ because the sets $(\mathbf{2}, 1)$ and $(\mathbf{3}, 2)$ do not contain beam 5, and similarly at $\mathbf{6}-\mathbf{5}$, since the sets $(\mathbf{5}, 4)$ and $(\mathbf{6}, 5)$ do not contain beam 2. Thus, in general, we will always obtain unusual covariances at the heights at which the distance between the North and the South beams corresponds to separation distances of $(n-1)\Delta x$, $n\Delta x$, and $(n+1)\Delta x$ (where n is odd, since for even n the North and South beams never intersect). Thus, if we now consider intersection points B (≈ 35 m) and C (≈ 173 m) in Fig. 10, then the separation distances are Δx and $5\Delta x$, respectively. Thus, we should expect unusual covariances at 0, Δx, and $2\Delta x$ at 35 m, whereas at 173 m, we expect the same at $4\Delta x$, $5\Delta x$, and $6\Delta x$.

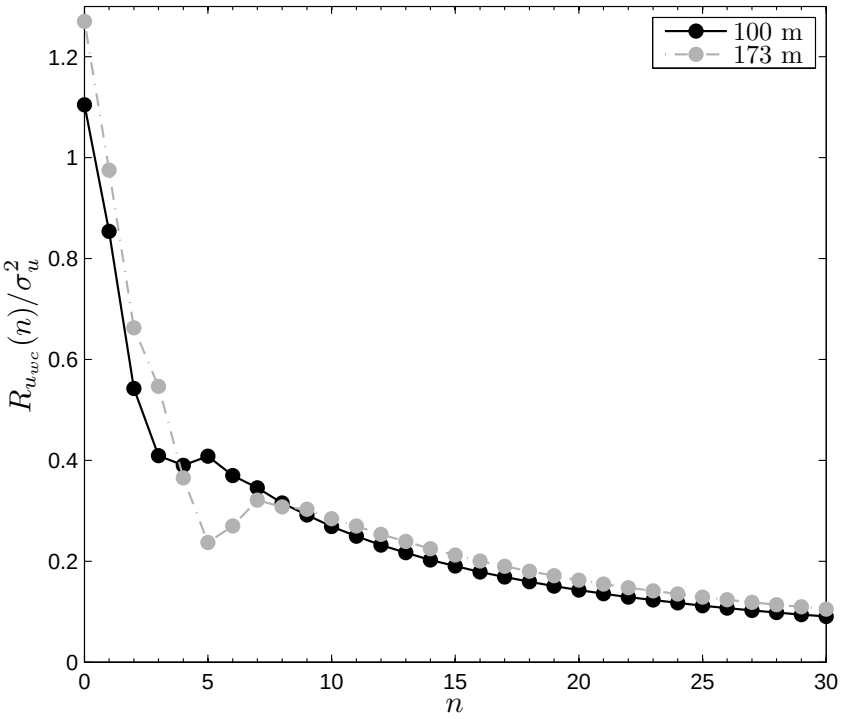

Figure 11: Comparison of $R_{u_{wc}}(n)/\sigma_u^2$ at different heights

In order to verify the above explanation, $R_{u_{wc}}(n)/\sigma_u^2$ (where σ_u^2 is the true variance of the u component) is calculated at two separation distances (100 and 173 m), as shown in Fig. 11. We do not calculate $R_{u_{wc}}(n)/\sigma_u^2$ at 35 m because the WindCube reliably measures from approximately 40 m (owing to a large measuring volume of about 30 m). σ_u^2 is calculated by integrating Eq. (65) over the k_1 domain at respective heights. We can now clearly see unusual covariances at $(n-1)\Delta x$, $n\Delta x$, and $(n+1)\Delta x$ at both heights, where $n = 3$ at 100 m and $n = 5$ at 173 m. Fig. 9 indicates that the model captures this beam interference phenomenon, which is also present in the measurements at 100 m, very well. Thus, it could also be implied that in nature, Taylor's hypothesis is valid to some extent.

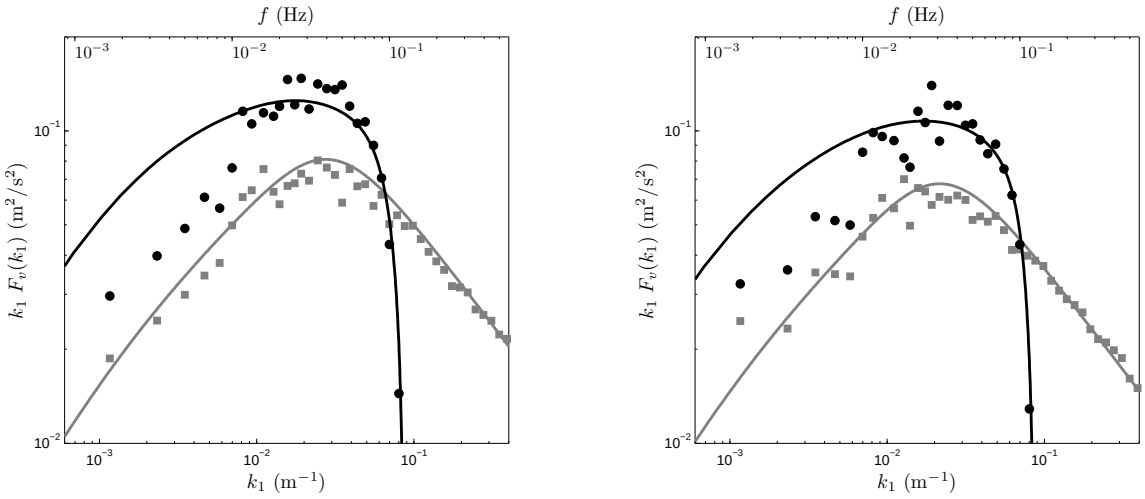

Figure 12: Comparison of the modeled and measured v spectrum at 60 m (left) and 100 m (right). The meaning of the symbols and colors correspond to those in Fig. 9

Fig. 12 shows the comparison of the modeled and measured v spectrum at 60 and 100m. As observed for the u component, the v spectrum measured by the lidar deviates significantly from that of the sonic spectrum. However, at very low wavenumbers, there is an offset in the spectral energy between the lidar and the sonic. The behavior in the inertial sub-range is the same as that for the u component, where a rapid attenuation in the spectral energy is observed. Our model agrees very well with the measurements at 60 and 100 m, except at very low wavenumbers ($< 0.005\ \mathrm{m}^{-1}$), where the model over estimates the spectral energy. One striking feature of this comparison is that as opposed to the u component, we do not see any beam interference phenomenon at 100 m because of Taylor's hypothesis. This is because only the E-W beams are used to deduce the v components, which are perpendicular to the mean wind field. Thus, even though we assume Taylor's hypothesis, the beams never interfere with each other at any separation distance. Thus, this result indirectly verifies the beam interference phenomenon explanation for the u component at 100 m. We give the following explanation for the over estimation of the spectral energy at very low wavenumbers.

From Eq. (64), it is understood that the v spectrum measured by the WindCube contains contributions from the v and w components of the spectral tensor, i.e., $\Phi_{22}(\boldsymbol{k})$ and $\Phi_{33}(\boldsymbol{k})$, weighted by the corresponding weighting functions $|\varphi(\boldsymbol{k}\cdot\boldsymbol{n}_E)|^2$ and $|\varphi(\boldsymbol{k}\cdot\boldsymbol{n}_W)|^2$. Due to the assumption of uniform shear and no effect of the Coriolis force by Mann (1994), the symmetry group of the spectral tensor model is such that the co-spectral energy between v and w is zero, i.e., $F_{23}(k_1) = 0$. We observed, using sonic anemometer measurements, that $F_{23}(k_1)$ is not exactly zero, but has some negative spectral energy at all wavenumbers. We also observed that $F_{23}(k_1) < F_{13}(k_1)$. On closely analyzing Eq. (64), we note that, in nature, if $F_{23}(k_1)$ contributes to the covariance measured by the lidar, it will result in overall reduction of $R_{v_{wc}}$. Thus, the symmetry group of Mann (1994) may not be entirely valid. We also find that the contribution of the second term in Eq. (64) is negligible, and only the first and the third terms add to the spectral energy. Let us now consider a case such that at 60 m, the beam is staring perpendicularly to the mean wind field in a horizontal plane. It will thus measure only the v component of the velocity field. In this case, the v spectrum measured by the WindCube is given as

$$F_{v_{wc*}}(k_1) = \int_{-\infty}^{\infty}\Big(\int_{-\infty}^{\infty}\Phi_{22}(\boldsymbol{k})\ dk_3\Big)|\hat{\varphi}(k_2)|^2\ dk_2, \tag{67}$$

where $*$ denotes spectra for a staring beam lidar. In Eq. (67), we first integrate over the k_3 domain, and the resulting two dimensional spectrum $E_v(k_1, k_2)$ is weighted by the filter function $|\hat{\varphi}(k_2)|^2$.

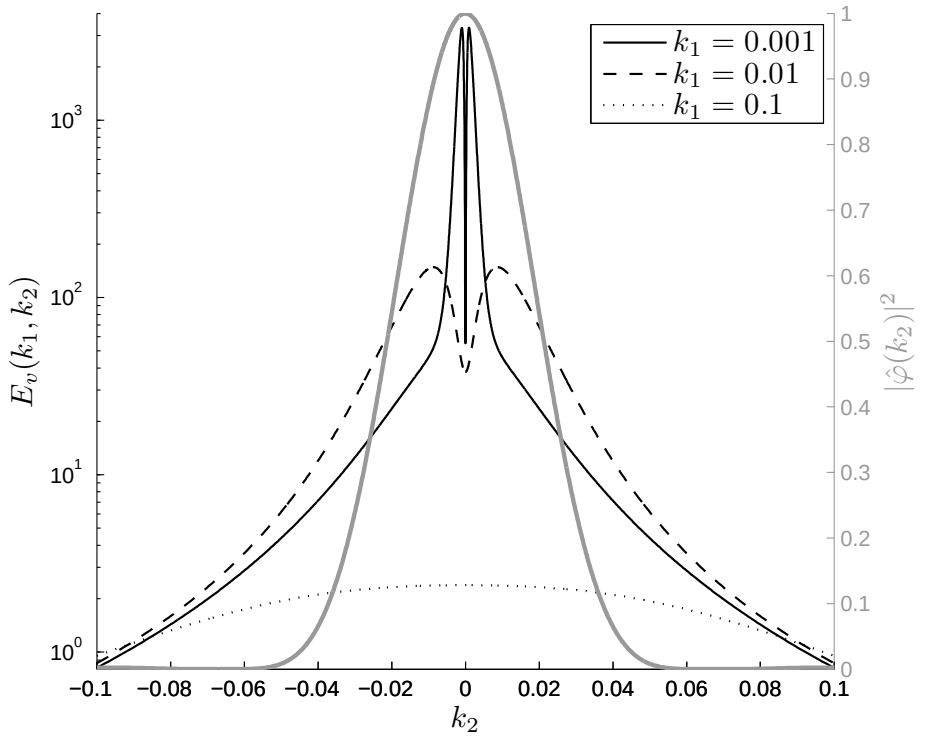

Figure 13: Two-Dimensional energy spectrum of the v component. The weighting function $|\hat{\varphi}(k_2)|^2$ is plotted on the right y-axis

The behavior of the weighting function is such that $|\hat{\varphi}(k_2)|^2 \to 1$ as $k_2 \to 0$. Thus, if the amount of two dimensional spectral energy increases sharply as $(k_1, k_2) \to 0$, then the contribution of this spectral energy in the one-dimensional spectrum will be significant. In order to verify this assumption, we calculate $E_v(k_1, k_2)$ at three values of k_1, i.e., $k_1 = (10^{-1}, 10^{-2}, 10^{-3})$ m^{-1}, as shown in Fig. 13. We also plot the variation of $|\hat{\varphi}(k_2)|^2$, so that filtering of the spectral energy for the respective wavenumbers is clearly evident. From the figure, it is observed that $k_1 \to 0$, $E_v(k_1, k_2)$ increases by several orders of magnitude with decreasing $|k_2|$ until a certain value of $|k_2|$, after which it decreases with $k_2 \to 0$. Since Mann (1994) does not assume isotropy in the horizontal plane, $E_v(k_1, k_2) \to 0$ as $(k_1, k_2) \to 0$ (Wyngaard, 2010). In our study, the WindCube is not horizontal, but at $\phi = 27.5°$ with the vertical. Hence, for the v component, the filter function along the line-of-sight acts over k_2 and k_3 domains. Its influence on averaging of the two and three dimensional spectral energy will be much more complicated than that for a horizontally pointing lidar. Nevertheless, we can argue similar reasons for the conically scanning case.

From the above explanation, we can consider four reasons for the over estimation of $F_{v_{wc}}(k_1)$ in the model as $k_1 \to 0$.

1. $E_v(k_1, k_2)$ could be more spread out such that the total energy over the k_2 domain would still be the same as that predicted by the Mann (1994) model.

2. The peak in $E_v(k_1, k_2)$ could be shifted to larger values of $|k_2|$.

3. Despite anisotropic conditions, $E_v(k_1, k_2)$ could approach zero as $(k_1, k_2) \to 0$.

4. There could be some contribution by $F_{23}(k_1)$.

As a consequence, the Mann (1994) model would still predict $F_v(k_1)$ considerably accurate. However, when $E_v(k_1, k_2)$ is weighted by $|\hat{\varphi}(k_2)|^2$, the total energy calculated using the Mann (1994) model and that obtained in nature would be different. Thus, it will cause overestimation of $F_{v_{wc}}(k_1)$ as $k_1 \to 0$, despite observing a good agreement between the theoretical and measured $F_v(k_1)$ (Fig. 12). Unfortunately, it is very difficult to measure the two- and three-dimensional spectra, and hence, we cannot verify our explanation.

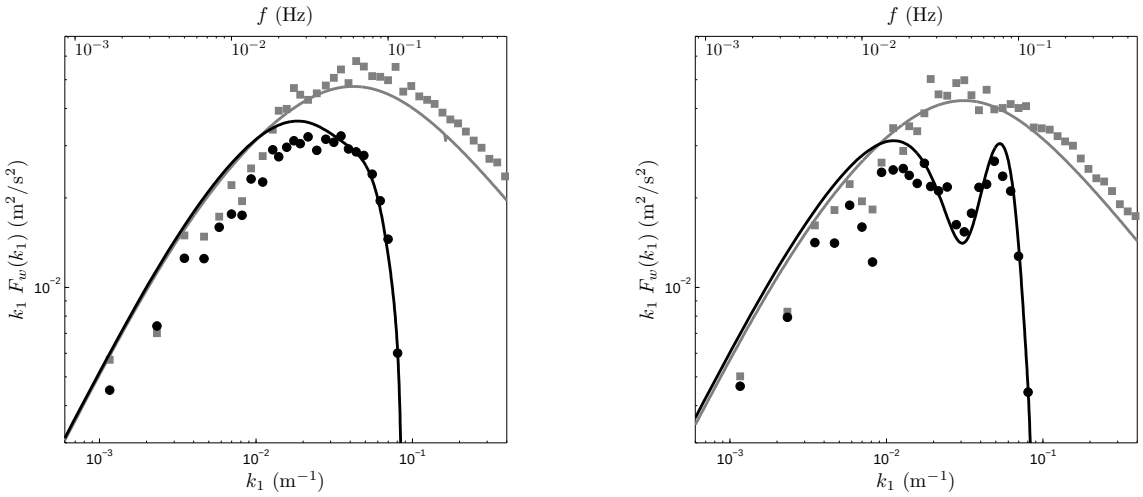

Figure 14: Comparison of the modeled and measured w spectrum at 60 m (left) and 100 m (right). The meaning of the symbols and colors correspond to those in Fig. 9

Fig. 14 shows the comparison of the modeled and measured w spectrum at 60 and 100 m. Since in the calculation of the w spectrum, we use only the North and South beams, we will obtain similar beam interference at 100 m, because of the assumption of Taylor's hypothesis, as that observed for the u spectrum. The measured WindCube spectrum agrees quite well with the model at both heights, especially at high wavenumbers. As observed for the u component, at 100 m we note the effect of unusual covariances on the spectral energies. At very low wavenumbers, there is a slight offset between the model and measurements. This offset could be because of the slight deviation in the modeled and measured sonic spectrum. The model also shows that at very low wavenumbers, because of very large turbulence eddies, the volume measurement from the lidar behaves similar to a point measurement.

3 Turbulence measurements using the six beam technique

In the previous section we have seen that the VAD technique results in large bias in the turbulence measurements. We are then forced to look at different ways of data analysis that do not give this bias. Instead of combining beams as in the VAD method, we instead use the variances of the radial velocities. Mathematically, it can be written as (Eberhard et al., 1989, Mann et al., 2010),

$$\begin{aligned}\langle v_r'^2 \rangle = &\langle u'^2 \rangle \sin^2\phi \cos^2\theta + \langle v'^2 \rangle \sin^2\phi \sin^2\theta + \langle w'^2 \rangle \cos^2\phi \\ &+ 2\langle u'v' \rangle \sin^2\phi \sin\theta \cos\theta + 2\langle u'w' \rangle \sin\phi \cos\phi \cos\theta + 2\langle v'w' \rangle \sin\phi \cos\phi \sin\theta\end{aligned} \tag{68}$$

where $\langle v_r'^2 \rangle$ is the radial velocity variance. Since there are six unknowns, we need six equations to solve for the set of the second-order moments,

$$\mathbf{\Sigma} = \Big(\langle u'^2 \rangle, \langle v'^2 \rangle, \langle w'^2 \rangle, \langle u'v' \rangle, \langle u'w' \rangle, \langle v'w' \rangle \Big) \tag{69}$$

Scanning the circle at only one half opening angle, using Eq. (68) there are infinite solutions for the set $\mathbf{\Sigma}$. Thus, we need more than one value of ϕ to obtain a solution for $\mathbf{\Sigma}$. The challenge is to obtain the optimum combination of $\boldsymbol{X} = (\theta_i, \phi_i)|_{i..6}$. If we represent Eq. (68) as a system of linear equations then in matrix form we can write,

$$\mathbf{\Sigma} = \boldsymbol{M^{-1}S} \tag{70}$$

where, $\boldsymbol{M}$ is a 6×6 matrix of the coefficients of $\mathbf{\Sigma}$, and $\boldsymbol{S} = \left(\langle {v'_{r_1}}^2 \rangle, \langle {v'_{r_2}}^2 \rangle, ..., \langle {v'_{r_6}}^2 \rangle\right)$ is the set of the variances of radial velocities. We then need to formulate some objective function based on minimizing the random errors in the measurements.

3.1 *Formulating the objective function*

The coordinate system for lidars is a left-handed coordinate system. In order to align with the mean wind direction, we need to apply coordinate transformations on any tensors that are defined in the original coordinate system. Thus, the second order tensor $\langle \mathrm{v}'_i \mathrm{v}'_j \rangle$ rotated clockwise in the mean wind direction has to be multiplied by a transformation matrix $\boldsymbol{T}$ given as,

$$\boldsymbol{T} = \begin{bmatrix} \cos\Theta & \sin\Theta & 0 \\ -\sin\Theta & \cos\Theta & 0 \\ 0 & 0 & 1 \end{bmatrix} \tag{71}$$

In the cartesian-tensor suffix notation, for a second-order tensor, we can write,

$$\langle \tilde{\mathrm{v}}'_k \tilde{\mathrm{v}}'_l \rangle = T_{ik} T_{jl} \langle \mathrm{v}'_i \mathrm{v}'_j \rangle \tag{72}$$

where $\langle \tilde{\mathrm{v}}'_i \tilde{\mathrm{v}}'_j \rangle$ are the second-order moments in the coordinate system rotated in the mean wind direction, and $T_{ik}T_{jl}$ are the direction cosines. Since $\langle \mathrm{v}'_i \mathrm{v}'_j \rangle$ is a symmetric second-order tensor, we are only interested in the set $\mathbf{\Sigma}$ given by Eq. 69. Using Einstein's summation, we get for each component of the set $\tilde{\mathbf{\Sigma}}$,

$$\langle \tilde{u'}^2 \rangle = \langle u'^2 \rangle \cos^2\Theta + \langle v'^2 \rangle \sin^2\Theta + \langle u'v' \rangle \sin 2\Theta \tag{73}$$

$$\langle \tilde{v'}^2 \rangle = \langle u'^2 \rangle \sin^2\Theta + \langle v'^2 \rangle \cos^2\Theta - \langle u'v' \rangle \sin 2\Theta \tag{74}$$

$$\langle \tilde{w'}^2 \rangle = \langle w'^2 \rangle \tag{75}$$

$$\widetilde{\langle u'v' \rangle} = -\frac{1}{2}\sin 2\Theta \langle u'^2 \rangle + \frac{1}{2}\sin 2\Theta \langle v'^2 \rangle + \langle u'v' \rangle \cos 2\Theta \tag{76}$$

$$\widetilde{\langle u'w' \rangle} = \langle u'w' \rangle \cos\Theta + \langle v'w' \rangle \sin\Theta \tag{77}$$

$$\widetilde{\langle v'w' \rangle} = -\langle u'w' \rangle \sin\Theta + \langle v'w' \rangle \cos\Theta \tag{78}$$

where $\tilde{\mathbf{\Sigma}} = \left(\langle \tilde{u'}^2 \rangle, \langle \tilde{v'}^2 \rangle, \langle \tilde{w'}^2 \rangle, \widetilde{\langle u'v' \rangle}, \widetilde{\langle u'w' \rangle}, \widetilde{\langle v'w' \rangle}\right)$ is the set of second-order moments in the coordinate system rotated in the mean wind direction. In matrix form, Eqs. (73–78) can be written as,

$$\begin{bmatrix} \langle \tilde{u'}^2 \rangle \\ \langle \tilde{v'}^2 \rangle \\ \langle \tilde{w'}^2 \rangle \\ \widetilde{\langle u'v' \rangle} \\ \widetilde{\langle u'w' \rangle} \\ \widetilde{\langle v'w' \rangle} \end{bmatrix} = \begin{bmatrix} \cos^2\Theta & \sin^2\Theta & 0 & \sin 2\Theta & 0 & 0 \\ \sin^2\Theta & \cos^2\Theta & 0 & -\sin 2\Theta & 0 & 0 \\ 0 & 0 & 1 & 0 & 0 & 0 \\ -\frac{1}{2}\sin 2\Theta & \frac{1}{2}\sin 2\Theta & 0 & \cos 2\Theta & 0 & 0 \\ 0 & 0 & 0 & 0 & \cos\Theta & \sin\Theta \\ 0 & 0 & 0 & 0 & -\sin\Theta & \cos\Theta \end{bmatrix} \begin{bmatrix} \langle u'^2 \rangle \\ \langle v'^2 \rangle \\ \langle w'^2 \rangle \\ \langle u'v' \rangle \\ \langle u'w' \rangle \\ \langle v'w' \rangle \end{bmatrix} \tag{79}$$

$$\tilde{\mathbf{\Sigma}} = \boldsymbol{R\Sigma} \tag{80}$$

where $\boldsymbol{R}$ is the transformation matrix to be applied on the set $\boldsymbol{\Sigma}$ to obtain $\tilde{\boldsymbol{\Sigma}}$ in the rotated coordinate system. Using Eq. (70), we can write,

$$\boldsymbol{\delta\tilde{\Sigma}} = \boldsymbol{RM}^{-1}\boldsymbol{\delta S} \tag{81}$$

where $\boldsymbol{\delta\tilde{\Sigma}}$ and $\boldsymbol{\delta S}$ are the random errors in the second-order moments and radial velocity variances respectively. Following lengthy manipulations, we get

$$\frac{\langle \boldsymbol{\delta\tilde{\Sigma}} \cdot \boldsymbol{\delta\tilde{\Sigma}} \rangle}{\langle \epsilon_s^2 \rangle} = Tr(\boldsymbol{RN}(\boldsymbol{RN})^T) \tag{82}$$

where $N = M^{-1}$, Tr denotes trace of a matrix, T denotes matrix transpose, and $\langle \epsilon_s^2 \rangle$ is the error variance of the radial velocities. In deriving Eq. (82) we have assumed that the error variance of the radial velocity is equal for all six beams. Eq. (82) states that the error variance is dependent on the mean wind direction. In order to make it independent of the mean wind direction, we assume a uniform distribution of the mean wind direction, and estimate the averaged ratio of the error variance. Thus,

$$\begin{aligned}\left\langle \frac{\langle \boldsymbol{\delta\tilde{\Sigma}} \cdot \boldsymbol{\delta\tilde{\Sigma}} \rangle}{\langle \epsilon_s^2 \rangle} \right\rangle &= \frac{1}{2\pi}\int_0^{2\pi} Tr(\boldsymbol{RN}(\boldsymbol{RN})^T)d\Theta \\ &= \frac{1}{2\pi}\int_0^{2\pi} Tr(\boldsymbol{RNN}^T\boldsymbol{R}^T)d\Theta\end{aligned}$$

Using the property of matrix trace that it is invariant under cyclic permutations we get,

$$\left\langle \frac{\langle \boldsymbol{\delta\tilde{\Sigma}} \cdot \boldsymbol{\delta\tilde{\Sigma}} \rangle}{\langle \epsilon_s^2 \rangle} \right\rangle = \frac{1}{2\pi}\int_0^{2\pi} Tr(\boldsymbol{R}^T\boldsymbol{RNN}^T)d\Theta \tag{83}$$

We can also switch the order between integration and matrix trace, i.e. either we can estimate the trace first and then the integration or vice-versa. Thus,

$$\left\langle \frac{\langle \boldsymbol{\delta\tilde{\Sigma}} \cdot \boldsymbol{\delta\tilde{\Sigma}} \rangle}{\langle \epsilon_s^2 \rangle} \right\rangle = Tr\left(\left[\frac{1}{2\pi}\int_0^{2\pi} \boldsymbol{R}^T\boldsymbol{R}d\Theta\right]\boldsymbol{NN}^T\right) \tag{84}$$

Solving the integral we get,

$$\left\langle \frac{\langle \boldsymbol{\delta\tilde{\Sigma}} \cdot \boldsymbol{\delta\tilde{\Sigma}} \rangle}{\langle \epsilon_s^2 \rangle} \right\rangle = Tr\left(\begin{bmatrix} \frac{7}{8} & \frac{1}{8} & 0 & 0 & 0 & 0 \\ \frac{1}{8} & \frac{7}{8} & 0 & 0 & 0 & 0 \\ 0 & 0 & 1 & 0 & 0 & 0 \\ 0 & 0 & 0 & \frac{3}{2} & 0 & 0 \\ 0 & 0 & 0 & 0 & 1 & 0 \\ 0 & 0 & 0 & 0 & 0 & 1 \end{bmatrix}\boldsymbol{NN}^T\right) \tag{85}$$

3.2 *Optimizing the objective function*

From (Eq. 85), it is clear that we need to optimize for 12 variables, i.e. a set $\boldsymbol{X} = (\theta_i, \phi_i)|_{i=1..6}$. The constraints constitute the range of angles of θ_i and ϕ_i. Thus, the optimization problem can be

stated as follows:

$$\text{Minimize } f(\boldsymbol{X}) = Tr\left(\begin{bmatrix} \frac{7}{8} & \frac{1}{8} & 0 & 0 & 0 & 0 \\ \frac{1}{8} & \frac{7}{8} & 0 & 0 & 0 & 0 \\ 0 & 0 & 1 & 0 & 0 & 0 \\ 0 & 0 & 0 & \frac{3}{2} & 0 & 0 \\ 0 & 0 & 0 & 0 & 1 & 0 \\ 0 & 0 & 0 & 0 & 0 & 1 \end{bmatrix} \boldsymbol{N}\boldsymbol{N}^T\right) \tag{86}$$

subject to constraints,

$0^\circ \leq \theta_i|_{i=1..6} \leq 360^\circ$

$0^\circ \leq \phi_i|_{i=1..6} \leq 45^\circ$

We assume that statistical homogeneity in the horizontal direction is valid only for a maximum value of $\phi_i = 45^\circ$ (Actually, this assumption is quite random, and depends on the terrain conditions). Analytical optimization of Eq. (86) provides a unique design solution set $\boldsymbol{X}$. However, Eq. (86) is a very complicated optimization problem, and hence, analytical solution is not possible[1]. In that case, the simplest method is to solve Eq. (86) for different combinations of $\boldsymbol{X}$. However, this would need very large number of computations. E.g. if we assume that $\boldsymbol{X}$ take only integer values, the number of computations required are $360^6 \times 90^6 \approx O(10^{27})$. It is observed that one computation of $f(\boldsymbol{X})$ takes approximately 0.5 seconds. Thus 10^{27} computations need approximately 10^{17} years. Moreover, if $\boldsymbol{X}$ also take real values then the number of computations, and hence, the time required increase manyfold. Thus, with the current available computer resources it is seen that evaluating $f(\boldsymbol{X})$ by directly substituting for different sets of $\boldsymbol{X}$ is not possible. We are thus forced to use available numerical optimization techniques.

There are two classes of numerical methods to solve a non-linear optimization problem Rao (2009):

1. Direct search methods
2. Gradient methods

For gradient methods, it is essential that the objective function is differentiable, and ∇f is defined at all points, i.e. $f(\boldsymbol{X})$ is not discontinuous Rao (2009). For simplicity we assume that $f(\boldsymbol{X})$ is discontinuous, and hence, we cannot use gradient methods. Thus, we optimize Eq. (86) using direct search methods only. The main advantage of using direct search methods is that they can be used for discontinuous and non-differentiable functions. The main limitation of such methods is that the found optimum may only be a local optimum.

In principle, any direct search algorithm can be used to find an optimum solution. It is generally very cumbersome to write algorithms for all available methods, and hence, we use the already available algorithms in Mathematica. For a global optimization problem, four different algorithms are available in Mathematica:

1. Simplex (NM) Nelder and Mead (1965)
2. Differential Evolution (DE) Storn and Price (1997)
3. Simulated Annealing (SA) Ingber (1993)
4. Random Search (RS) Rao (2009)

Eventually, we have to choose a solution set from one of these algorithms.

Table 2 gives a comparison of different optimization methods, when $\boldsymbol{X}$ is constrained to take real values. It is observed that the NM, SA and RS methods give the same optimum $f(\boldsymbol{X}^*)$. The

[1]Corresponding attempt is made in Mathematica

Table 2: Comparison of the optimization methods

Optimization Methods								
	Nelder-Mead		Differential Evolution		Simulated Annealing		Random Search	
$\langle \boldsymbol{\delta\Sigma} \cdot \boldsymbol{\delta\Sigma} \rangle / \langle \epsilon_s^2 \rangle$	10.2		11.78		10.2		10.2	
i	θ_i	ϕ_i	θ_i	ϕ_i	θ_i	ϕ_i	θ_i	ϕ_i
1	0	45	0	44.9999	0	45	0	45
2	284.451	1.087e-7	109.771	0.00087255	72	45	216	45
3	144	45	233.185	43.8284	297.23	6.8733e-6	143.035	6.6121e-15
4	288	45	310.453	44.9993	216	45	144	45
5	72	45	144.495	44.9333	288	45	72	45
6	216	45	89.3294	44.9993	144	45	288	45

DE method gives a slightly higher value of the optimum. $\boldsymbol{X}$ is evaluated to machine precision. However, in reality it is difficult to orient the laser beam at such precise angles ϕ_i. Hence, we rounded $\boldsymbol{X^*}$ to the nearest integer values and checked its influence on $f(\boldsymbol{X^*})$. We found that there is no influence of rounding of $\boldsymbol{X^*}$ on $f(\boldsymbol{X^*})$.

3.3 *Results*

Following Eq. (70) we can estimate the second-order moments using the six beam approach. We choose $\boldsymbol{X}$ from the SA method. Since the NM and RS methods also give the same optimum solution, $\boldsymbol{X}$ could also be chosen from these methods. From Eq. (81) the u variance can be written as,

$$\langle \tilde{u'}^2 \rangle = \langle {v'}^2_{r_1} \rangle - \langle {v'}^2_{r_3} \rangle - 0.085 \left(\langle {v'}^2_{r_2} \rangle + \langle {v'}^2_{r_5} \rangle \right) + 0.585 \left(\langle {v'}^2_{r_4} \rangle + \langle {v'}^2_{r_6} \rangle \right) \tag{87}$$

Following section 2.1 we get,

$$\langle {v'}^2_{r_1} \rangle = \int \Phi_{ij}(\boldsymbol{k}) \beta_{i1}(\boldsymbol{k}) \beta^*_{j1}(\boldsymbol{k}) d\boldsymbol{k} \tag{88}$$

where $\beta_{i1}(\boldsymbol{k}) = \left(\int_{-\infty}^{\infty} \varphi(s) n_{i1} e^{\mathrm{i}(s+d_f)\boldsymbol{k}\cdot\boldsymbol{n_1}} ds \right)$ and $*$ denotes complex conjugation. We can then use appropriate weighting function $\varphi(s)$ to estimate $\beta_{i1}(\boldsymbol{k})$. We can estimate the variances of the radial velocities in the remaining beam directions in a similar manner and substitute in Eq. (87) to theoretically estimate the u variance measured by the lidar. The remaining second-order moments are estimated in a similar manner.

Fig. (15) shows theoretical comparison of the systematic errors using the six beam approach with that using the VAD technique. Although the results are obtained for all stability conditions, only the neutral conditions are shown. One striking difference between two approaches is that the systematic error in the w variance is reduced significantly using the six beam approach. This is mainly because we have one vertical beam, and the only form of bias that remains is the volume averaging. For the ZephIR, the systematic errors in u and v variances are the same for both approaches. For the Windcube, a significant improvement is obtained for all variances using the six beam approach. Although, fig. (15b) shows that the VAD technique gives lower systematic error, it is mainly due to the addition and subtraction of all second-order moments. This effect is completely eliminated using the six beam approach. The only form of bias that remains is then the line-of-sight averaging. It has been observed that the Windcube systematic errors remain constant for the neutral and unstable conditions (not shown) using the six beam approach. Such is not the case with the VAD technique, where there is an over estimation of the variances.

4 Summary

From section 2 it is clear that VAD technique should not be used in turbulence measurements using lidars as it results in large systematic errors. Two mechanisms contribute to the systematic errors,

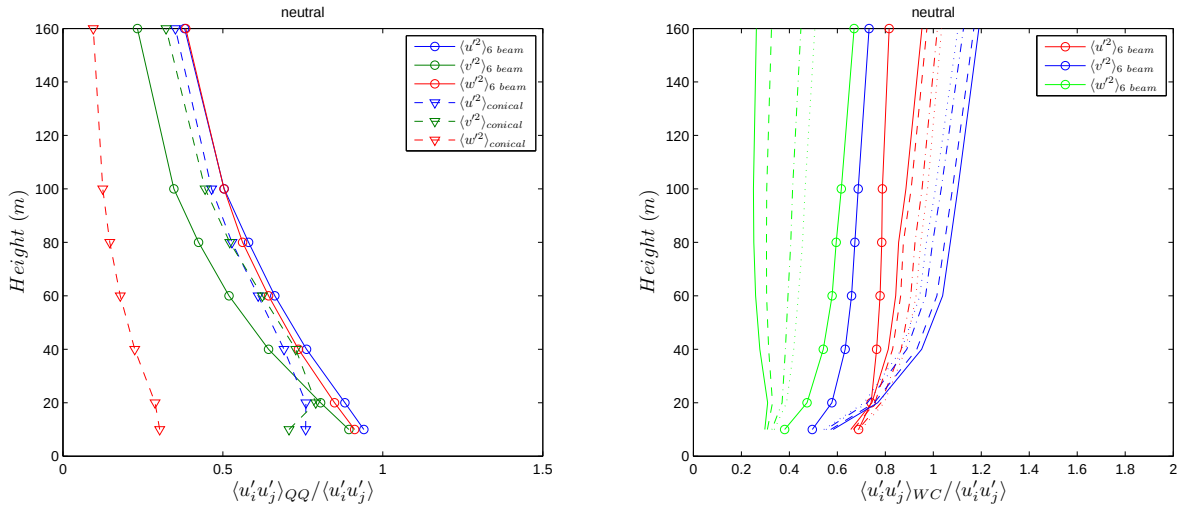

(a) ZephIR (b) Windcube

Figure 15: Comparison of the ZephIR and Windcube systematic errors under neutral conditions using the six Beam approach and the VAD technique

1. averaging of turbulence within the sample volume, and
2. contribution of other components of R_{ij}

Also, from Eqs. (15, 18, 19 and 44) the general lidar equation for the second-order moments using the VAD data processing technique can be written as,

$$\langle \mathrm{v}_m' \mathrm{v}_n' \rangle_{lidar} = \int \Phi_{ij}(\boldsymbol{k}) X_i{}^m(\boldsymbol{k}) Y_j^{*n}(\boldsymbol{k})\, d\boldsymbol{k}; \tag{89}$$

$$X_i{}^m(\boldsymbol{k}) = \left\{ \begin{array}{ll} \beta_i(\boldsymbol{k}) \bigwedge b_i(\boldsymbol{k}), & m=1 \\ \gamma_i(\boldsymbol{k}) \bigwedge c_i(\boldsymbol{k}), & m=2 \\ \alpha_i(\boldsymbol{k}) \bigwedge a_i(\boldsymbol{k}), & m=3 \end{array} \right\} \quad , \quad Y_j^{*n}(\boldsymbol{k}) = \left\{ \begin{array}{ll} \beta_j^*(\boldsymbol{k}) \bigwedge b_j^*(\boldsymbol{k}), & n=1 \\ \gamma_j^*(\boldsymbol{k}) \bigwedge c_j^*(\boldsymbol{k}), & n=2 \\ \alpha_j^*(\boldsymbol{k}) \bigwedge a_j^*(\boldsymbol{k}), & n=3 \end{array} \right\}$$

The weighting functions $\alpha_i(\boldsymbol{k})$, $\beta_i(\boldsymbol{k})$, $\gamma_i(\boldsymbol{k})$ are used for the ZephIR and $a_i(\boldsymbol{k})$, $b_i(\boldsymbol{k})$, $c_i(\boldsymbol{k})$ are used for the WindCube. Thus, the measurement of the second-order moment by lidar involves interaction of all components of the spectral velocity tensor $\Phi_{ij}(\boldsymbol{k})$ weighted by the corresponding weighting functions $X_i{}^m(\boldsymbol{k})$ and $Y_j^{*n}(\boldsymbol{k})$. It is to be noted that Eqn. (89) is given in Einstein summation convention, and hence, in order to explicitly see the contribution of all components of $\Phi_{ij}(\boldsymbol{k})$ on the measurement of the second-order moments by lidar, this equation must be expanded for all values of the subscripts i and j. In most cases, this results in the attenuation of the second-order moments, whereas in some cases this also results in amplification of the second-order moment, e.g. as observed for the WindCube in the unstable conditions (see Fig. 7).

One might argue that in order to retrieve true turbulence we can simply use the ratio between the lidar and sonic measured R_{ij}, but the results in section 2.2 demonstrate that it is not possible. A simple transfer function in the spectral domain cannot simply be deduced because of complex interaction of the components of R_{ij}. Unfortunately, in many research studies consideration to such systematic errors is not given and advanced studies are further carried out, leading to wrong interpretation of results. A concerted effort is therefore required in the remote sensing community to find methods that result in unbiased measurement of turbulence. The six beam approach is one such method that has the potential to serve this purpose.

References

B. Canadillas, A. Bégué, and T. Neumann. Comparison of turbulence spectra derived from LiDAR and sonic measurements at the offshore platform FINO1. In *DEWEK 2010,* 10^{th} *German Wind Energy Conference*, 2010.

W L. Eberhard, R E. Cupp, and K R. Healy. Doppler lidar measurements of profiles of turbulence and momentum flux. *Journal of Atmospheric and Oceanic Technology*, 6:809–819, 1989. doi: 10.1175/1520-0426(1989)006¡0809:DLMOPO¿2.0.CO;2.

A C. Genz and A A. Malik. Remarks on algorithm 006: An Adaptive Algorithm for Numerical Integration over an N-dimensional Rectangular Region. *Journal of Computational and Applied Mathematics*, 6(4):295–302, 1980. doi: 10.1016/0771-050X(80)90039-X.

S-E. Gryning, E. Batchvarova, B. Brümmer, H. Jørgensen, and S. Larsen. On the extension of the wind profile over homogeneous terrain beyond the surface layer. *Boundary-Layer Meteorology*, 124(2):251–268, 2007. doi: 10.1007/s10546-007-9166-9.

L. Ingber. Simulated annealing: Practice versus theory. *Mathematical Computer Modelling*, 18(11): 29–57, 1993.

J C. Kaimal and J J. Finnigan. *Atmospheric Boundary Layer Flows*, chapter Acquisition and processing of atmospheric boundary layer data, pages 255–257. Number 7. Oxford University Press, New York, 1994.

D H. Lenschow, J. Mann, and L. Kristensen. How long is long enough when measuring fluxes and other turbulence statistics? *Journal of Atmospheric and Oceanic Technology*, 11:661–673, 1994.

P. Lindelöw. *Fibre Based Coherent Lidars for Remote Wind Sensing.* PhD thesis, Technical University Denmark, 2007.

P. Lindelöw-Marsden. UpWind D1. Uncertainties in wind assessment with LIDAR. Technical Report Risø-R-1681(EN), Risø DTU, 2009.

J. Mann. The spatial structure of neutral atmospheric surface-layer turbulence. *Journal of Fluid Mechanics*, 273:141–168, 1994. ISSN 0022-1120. doi: 10.1017/S0022112094001886.

J. Mann, A. Peña, F. Bingöl, R. Wagner, and M S. Courtney. Lidar scanning of momentum flux in and above the surface layer. *Journal of Atmospheric and Oceanic Technology*, 27(6):792–806, 2010. doi: 10.1175/2010JTECHA1389.1.

A S. Monin and A M. Yaglom. *Statistical Fluid Mechanics*, volume 2. MIT Press, 1975.

M. Motta and R J. Barthelmie. The influence of non-logarithmic wind speed profiles on potential power output at Danish offshore sites. *Wind Energy*, pages 219–236, 2005. doi: 10.1002/we.146.

J A. Nelder and R. Mead. A simplex method for function minimization. *The computer Journal*, 7: 308–313, 1965.

A. Peña, S-E. Gryning, and J. Mann. On the length scale of the wind profile. *Quarterly Journal of the Royal Meteorological Society*, 136(653):2119–2131, 2010. doi: 10.1002/qj.714.

S. Rao. *Engineering Optimization: Theory and Practice.* John Wiley and Sons Inc., Hoboken, New Jersey, fourth edition, 2009. ISBN 978-0-470-18352-6.

C M. Sonnenschein and F A. Horrigan. Signal-to-noise relationships for coaxial systems that heterodyne backscatter from atmosphere. *Applied optics*, 10(7):1600, 1971.

R. Storn and K. Price. Differential evolution a simple and efficient heuristic for global optimization over continuous spaces. *Journal of Global Optimization*, 11(4):341–359, 1997.

J C. Wyngaard. *Turbulence in the Atmosphere*. Cambridge University Press, New York, 2010. ISBN 978-0-521-88769-4.